Journal of the Mechanics and Physics of Solids 61 (2013) 579–596

Contents lists available at SciVerse ScienceDirect

Journal of the Mechanics and Physics of Solids

journal homepage: www.elsevier.com/locate/jmps

Stress relaxation through interdiffusion in amorphous lithium alloy electrodes

Y.F. Gao [a], M. Cho [b], M. Zhou [a,b,*]

[a] The George W. Woodruff School of Mechanical Engineering, Georgia Institute of Technology, Atlanta, GA 30332-0405, USA
[b] WCU Program on Multiscale Mechanical Design, School of Mechanical and Aerospace Engineering, Seoul National University, Seoul, Korea

ARTICLE INFO

Article history:
Received 2 December 2011
Received in revised form
31 May 2012
Accepted 3 September 2012
Available online 11 September 2012

Keywords:
Li-ion battery
Stress relaxation
Interdiffusion
Mixed finite element

ABSTRACT

At high guest (lithium) atom concentrations, the diffusion of host (e.g., silicon) atoms may become significant in amorphous Li-alloy-based solid electrodes. The effect of this diffusion mechanism on stress development is in addition to guest atom diffusion, stress-induced enhancement of guest atom diffusion and plasticity. The effect of the diffusive migration of host atoms in amorphous Li-alloy-based electrodes is investigated using a continuum model. A mixed-form finite element framework is developed to simulate the full coupling between stress development and interdiffusion. This framework overcomes the challenges associated with the numerical evaluation of the hydrostatic stress gradient. The analysis focuses on the relative importance of the mechanical driving force and chemical driving force for host migration. Calculations show that host migration can cause stress reductions of up to ~20% in Li–Si electrodes at stress levels below the yield threshold of the material. Analyses also show that the long-term steady state of stress distribution is independent of the host diffusivity and the thermodynamic factor of diffusion which quantifies the tendency of the two species of atoms to chemically mix, even though the transient behavior (in particular, the peak stresses during charging being important quantities) does depend on the thermodynamic factor and the host diffusivity. The diffusion of Si (host) introduces a time scale which, along with the time scale for Li (guest) diffusion, controls the diffusional response of electrodes.

1. Introduction

In the quest for better Li-ion batteries, Li alloys have attracted significant interest since they offer greater specific and volumetric capacities than graphite. One of the main challenges with alloy-based Li-ion battery electrodes, however, has been the large volume changes and associated cracking during lithiation and delithiation (Beaulieu et al., 2003; Larcher et al., 2007; Sethuraman et al., 2010). One way to mitigate the problem is to reduce the size of the electrodes. In particular, electrodes made of nano-sized structures such as nanowires (NWs), nanotubes and nanoscale core-shell structures have been shown to be particularly effective in avoiding fracture (Chan et al., 2008; Cui et al., 2009; Hu et al., 2011; Magasinski et al., 2010; Song et al., 2010). In many cases, nanosized electrodes show no tendency to fracture and instead degrade

* Corresponding author at: The George W. Woodruff School of Mechanical Engineering, Georgia Institute of Technology, Atlanta, GA 30332-0405, USA. Tel.: +1 404 894 3294; fax: +1 404 894 0186.
E-mail addresses: min.zhou@gatech.edu, min.zhou@me.gatech.edu (M. Zhou).

0022-5096/$ - see front matter © 2012 Elsevier Ltd. All rights reserved.
http://dx.doi.org/10.1016/j.jmps.2012.09.004

through failure mechanisms which are distinctly different from those in electrodes of larger sizes. For example, while bulk and thin film Si electrodes mainly fail through cracking (Beaulieu et al., 2001, 2003), nano-sized Si electrodes degrade through internal nano-pore formation or surface roughening (Choi et al., 2010; Hu et al., 2011). Void formation rather than fracture has also been observed in Li/Ge nanowire electrodes (Liu et al., 2011a).

The transition of failure through fracture to degradation through void formation and surface roughening in the cases cited occurs due to a number of reasons. Although many mechanisms are responsible, primary factors include concentration-induced material softening (e.g., reductions in elastic modulus and yield threshold) and stress relaxation through several mechanisms. The latter plays a very important role as lower stresses reduce the likelihood of cracking and allow higher charging rates to be achieved. Obviously, identification and quantification of stress buildup and relaxation mechanisms are especially relevant to the study of electrode performance and reliability.

Three mechanisms lead to stress buildup when a Li-alloy electrode is charged or discharged. The first mechanism arises due to the inhomogeneity of Li concentration. When lithium is inserted through the surface, a gradient of Li concentration develops in the material, leading to inhomogeneous expansion which causes stress development. The stresses in this scenario depend on the ratio between the time scale for diffusion ($\sim \rho_0^2/D_{eff}^{Li}$) and the total time to attain full charging. Here, ρ_0 is the characteristic size scale of the electrode particle and D_{eff}^{Li} is the effective diffusivity of Li (Christensen and Newman, 2006; Gao and Zhou, 2011). The second mechanism has to do with constraint applied by the current collector or a solid–electrolyte interface (SEI) layer, as observed in thin-film electrodes (Li et al., 2011; Xiao et al., 2011) or CNT-Si core-shell structures (Hu et al., 2011). The third mechanism, mainly seen during the first charging cycle of crystalline silicon electrodes, is due to the mismatch strain at lithiated/unlithiated phase boundaries (Chon et al., 2011; Liu et al., 2011b). Relief of the combined stresses due to the three mechanisms is a primary concern in the design of electrodes.

Many continuum studies have been carried out to investigate the buildup and mitigation of stresses in Li-ion battery electrodes and the associated effects on the electrochemistry (Cheng and Verbrugge, 2008; Christensen and Newman, 2006; Cogswell and Bazant, 2012; Garcia et al., 2005; Haftbaradaran et al., 2010; Kao et al., 2010; Purkayastha and McMeeking, 2012; Ryu et al., 2011; Van der Ven et al., 2009; Zhang et al., 2007). Tang et al. (2010a, 2010b) showed that the elastic strain energy can significantly affect the electrochemistry in the cathode material of $LiFePO_4$. Bower et al. (2011) developed a comprehensive framework and used it to analyze the time-dependent plasticity in thin-film Li/Si electrodes. The effect of stress-enhanced diffusion (SED) was analyzed, revealing significant reduction in stress due to the mechanical driving force to diffusion (Gao and Zhou, 2011). Deshpande et al. (2010) considered the effect of surface stresses and concluded that surface effect can reduce the tensile stresses in nano-sized electrodes, thereby improving electrode cyclability. Zhao et al. (2011a) considered plastic deformation and showed that inelastic flow can significantly alleviate the stresses in Li/Si. The mechanisms for stress reduction considered in these analyses include stress-enhanced diffusion of Li, surface-effect-induced compressive stresses and plasticity.

One of the stress reduction mechanisms in Li–Si that have not been analyzed is the migration of Si (host) atoms which can be significant especially at high Li concentrations when the bonds between Si atoms are weakened or broken. Indeed, DFT calculations by Kim et al. (2011) show that the bonding environment of silicon atoms changes significantly as lithium concentration increases, indicating that the diffusive migration of silicon may become non-negligible. Recently, Johari et al. (2011) calculated the diffusivity of both Li and Si (D^{Li} and D^{Si}) in crystalline and amorphous Si (c-Si and a-Si) electrodes using ab initio molecular dynamics. They found that $D^{Li}=1.67\times10^{-10}$–$4.88\times10^{-9}\ cm^2\ s^{-1}$ and $D^{Si}=1.97\times10^{-14}$–$5.74\times10^{-13}\ cm^2\ s^{-1}$ for c-Si and $D^{Li}=1.25\times10^{-9}$–$3.69\times10^{-8}\ cm^2\ s^{-1}$ and $D^{Si}=1.53\times10^{-11}$–$5.13\times10^{-10}\ cm^2\ s^{-1}$ for a-Si. The associated diffusivity ratio in a-Si falls into the range of $D^{Si}/D^{Li}=0.8\times10^{-2}$–$1.39\times10^{-2}$. It should be noted that the study by Johari et al. was conducted on Li/Si systems with the composition of $Li_{1.0}Si$. For higher Li contents, the diffusivity ratio D^{Si}/D^{Li} could be even higher since more Si–Si covalent bonds are broken. In Li/Ge, another promising alloy-based electrode material, host diffusion could be even more significant since the Ge–Ge covalent bond is much weaker than the Si–Si bond (the melting temperatures of crystalline Si and Ge are 1687 K and 1211.40 K, respectively).

In this paper, a numerical framework with mixed finite elements is developed to analyze the strong coupling between stress development and interdiffusion in Li-alloy based electrodes with finite host diffusivity. The analysis focuses on the direction of the diffusive migration of host (Si) atoms and the dependence of the direction on the relative strengths of the chemical and mechanical driving forces. A parametric study is carried out over a range of values of host diffusivity and the thermodynamic factor which measures the tendency for the Li and Si atoms to chemically mix. In particular, the analysis allows the effect of Si diffusion on stress evolution to be quantified. The calculations also focus on the time scales associated with the diffusive migration of guest and host, and how these time scales affect the evolution and distributions of stresses and concentrations, especially at charge times beyond the characteristic time scale for host migration. The results will show quantitatively that the diffusion of Si is a significant mechanism for stress relief in Li/Si, in addition to SED and inelastic deformation. Of particular interest is the finding that the steady-state distributions of stresses at times much longer than the characteristic time for Si diffusion depends on neither the thermodynamic factor nor the diffusivity of Si.

2. Theoretical framework for deformation–interdiffusion coupling

The electrode is assumed to be composed of two chemical species: host (denoted as H) and guest (denoted as G, being lithium in this paper). Vacancies are not treated as a chemical species due to the lack of site-conservation constraint in

amorphous materials (Stephenson, 1988; Van der Ven et al., 2010). Sufficient electric conductance is assumed so that the whole electrode has a uniform electric potential, and only the deformation and diffusion processes need to be analyzed explicitly.

2.1. Kinematics

Since the material of interest is highly amorphous with small but non-zero host diffusivity (Johari et al., 2011; Kim et al., 2011), the notion of continuous deformation must be used with caution. Following the treatment by Stephenson (1988), we identify two types of host atom movement during guest (lithium) insertion: collective convection and diffusive transport. To illustrate the relative displacement between neighboring host atoms, network lines (solid black) linking adjacent hosts are introduced in Fig. 1. It should be noted that these lines do not necessarily represent host–host bonds, although recent studies do indicate that a significant portion of Si atoms tends to remain in rings, chains or pairs even in highly lithiated amorphous Li/Si (Kim et al., 2011). It should also be noted that the regular arrangement of the initial network [Fig. 1(a)] is used only to facilitate the illustration without implying any regularity or periodicity in atomic structure. As the material expands due to guest insertion, two scenarios may arise in terms of the movement of the host atoms. In the first scenario (consider atom B as the example), the network lines linking the host atom (B) with its neighbors (B–C, B–D, B–E) remain; and the movement of the host (B) can be tracked by bookkeeping the continuum deformation $\mathbf{x}=\mathbf{x}(\mathbf{X},t)$ of the network. We call this type of host movement collective convection. In the second scenario (consider atom A as the example), the local distortion of the network is so significant that the atom's nearest neighbors completely change. The displacement of atom A can be decomposed into two parts: the first part is from the initial position of A to an imaginary point A′ and is due to collective convection; the second part is from A′ to the final position of A. The second part of displacement (from A′ to the final position) is highly random compared with the collective convection, and the effect is the diffusive transport of the host atom relative to the collectively deformed configuration. Here, the position of A′ can be obtained by averaging the positions of atoms within a representative volume element (RVE) around A [A, C, D, F and G in Fig. 1(a)]. The deformed network so obtained (to which A′ is attached) reflects the structural deformation of the material and defines the updated Lagrangian configuration.

If the diffusive transport dominates the host atom movement, the arrangement of the hosts is reshuffled quickly (too many host atoms move like A) and a continuum mapping $\mathbf{x}=\mathbf{x}(\mathbf{X},t)$ between the reference and current configurations may not be well-defined. Here, we assume that the diffusivity of the hosts is much smaller than that of the guests (Li) so that the host network can be identified and, consequently, the continuous deformation $\mathbf{x}=\mathbf{x}(\mathbf{X},t)$ is well-defined. Note that $\mathbf{x}=\mathbf{x}(\mathbf{X},t)$ should be construed in an average sense which may involve statistically averaging the displacement of atoms in a specific RVE [cf. Fig. 1].

The Eulerian concentrations (concentrations in the current configuration) of the host (e.g., Si) and guest (lithium), namely the atomic numbers per unit current volume, are denoted by c^H and c^G, respectively. Their Lagrangian counterparts C^H and C^G in the reference configuration are related to c^H and c^G by $C^H=\det(\mathbf{F})c^H$ and $C^G=\det(\mathbf{F})c^G$, with $F=\partial x/\partial X$ being the deformation gradient. The dimensionless compositions $x^H\equiv c^H/(c^G+c^H)$, $x^G\equiv c^G/(c^G+c^H)$ and $\xi\equiv c^G/c^H$, on the other hand, can be used to measure the proportions of the concentrations of the host and the guest.

It is well-known that Li/Si may undergo plastic deformation when the stresses reach the yielding threshold (Hertzberg et al., 2011; Sethuraman et al., 2010). Since the major issue of interest in this paper is the effect of mobile host atoms in amorphous Li-alloy electrodes, we assume that the stresses are below the yielding threshold in order to simplify the theory and concentrate on the coupling between deformation and interdiffusion. This also allows the effect of host diffusion to be

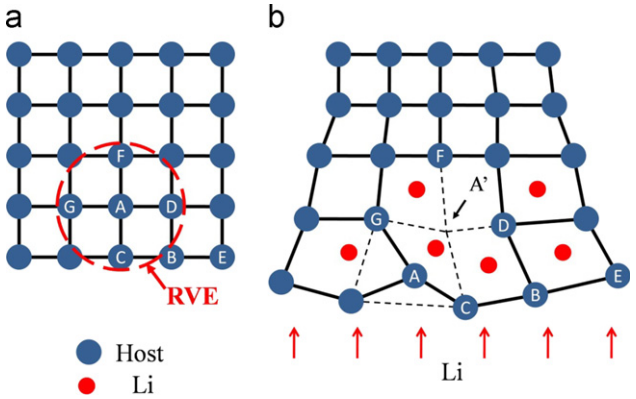

Fig. 1. The distinction between collective convection and diffusive transport. (a) The original host network. The solid black lines represent the network lines linking each host atoms to its neighboring hosts. These network lines do not necessarily represent host–host bonds. (b) When guest atoms (Li here) are inserted, the host network is distorted and some host atoms (e.g. atom A) may migrate relative the network. The dashed lines in (b) gives the host network site A′ which is given by averaging the movement of atoms (i.e. A, C, D, F and G) in a RVE around A.

better quantified. The deformation gradient under this condition can be decomposed as (Lee, 1981)

$$\mathbf{F}=\mathbf{F}^{e}\cdot\mathbf{F}^{SF}, \tag{1}$$

where $\mathbf{F}^{e}$ and $\mathbf{F}^{SF}$ are the parts of the deformation gradient associated with elastic deformation and stress-free expansion due to concentration changes, respectively (Bower et al., 2011; Swaminathan et al., 2007; Wu, 2001; Zhou et al., 2010). The associated rates of deformation, on the other hand, are

$$\left.\begin{aligned}&\mathbf{D}^{e}\equiv[\dot{\mathbf{F}}^{e}(\mathbf{F}^{e})^{-1}]_{sym},\\&\mathbf{D}^{SF}\equiv[\mathbf{F}^{e}\cdot\dot{\mathbf{F}}^{SF}\cdot(\mathbf{F}^{SF})^{-1}\cdot(\mathbf{F}^{e})^{-1}]_{sym},\quad \textit{and}\\&\mathbf{D}\equiv[\dot{\mathbf{F}}\mathbf{F}^{-1}]_{sym}=\mathbf{D}^{e}+\mathbf{D}^{SF}.\end{aligned}\right\} \tag{2}$$

2.2. Conservation of mass and momentum

The diffusive fluxes of guest and host can be measured either in the Lagrangian frame as $\mathbf{J}^{G}$ and $\mathbf{J}^{H}$ or in the updated Lagrangian frame as $\mathbf{j}^{G}$ and $\mathbf{j}^{H}$. These quantities are related through $\mathbf{f}\equiv\mathbf{F}^{-1}$ as

$$J_{K}^{S}=\det(\mathbf{F})f_{Ki}j_{i}^{S}\quad(S=G,\ H). \tag{3}$$

The associated equation for mass conservation in the Lagrangian frame is

$$\frac{\partial C^{S}}{\partial t}+\frac{\partial J_{K}^{S}}{\partial X_{K}}=R_{b}^{S}\quad(S=G,\ H), \tag{4}$$

where R_{b}^{S} is the body source of species S ($=G,H$) measured in the Lagrangian frame. In this paper, we assume $R_{b}^{G}=R_{b}^{H}=0$.

It is important to notice that $\mathbf{j}^{G}$ and $\mathbf{j}^{H}$ are measured in the updated Lagrangian frame relative to the moving host network which undergoes convection $\mathbf{x}=\mathbf{x}(\mathbf{X},t)$, instead of in the Eulerian frame. If the fluxes were to be measured relative to the Eulerian frame, the conservation of mass would take the form of a mixed convection–diffusion equation in order to avoid double counting the movement of G and H (Stephenson, 1988). That approach is not used here. Again, vacancies should not be treated as a chemical species here due to the lack of site-conservation constraint in amorphous materials, as discussed by Stephenson (1988).

Finally, under the conditions of zero body force and negligible inertia effect, balance of momentum takes the form

$$\frac{\partial\sigma_{ji}}{\partial x_{j}}=0, \tag{5}$$

where σ_{ij} is the mechanical Cauchy stress. Contributions due to the electromagnetic Maxwell stress is neglected since its magnitude is much smaller than the contribution due to σ_{ij} in typical battery electrode applications (Bower et al., 2011).

2.3. Thermodynamics

The thermodynamic properties of the electrode material can be characterized by the Lagrangian density of the Helmholtz free energy ϕ (Wu, 2001). We assume

$$\phi=\phi(\mathbf{F}^{e},C^{H},C^{G},\theta,\alpha), \tag{6}$$

where θ is the temperature and α is an internal state variable describing the non-equilibrium metastable states. Physically, α can be the degree of amorphization (Argon and Demkowicz, 2008; Limthongkul et al., 2003), porosity (Choi et al., 2010), or degree of damage. Consider an infinitesimal reversible virtual deformation $\delta\mathbf{x}$ during which C^{H}, C^{G}, θ and α are kept constant, the virtual work done by the external agent is related to the first Piola–Kirchhoff stress $\sigma_{Kj}^{PK1}=\det(\mathbf{F})f_{Ki}\sigma_{ij}$ through

$$\delta W_{mech}=\int_{V_{0}}\sigma_{Kj}^{PK1}\frac{\partial\delta x_{j}}{\partial X_{K}}dV_{0}, \tag{7}$$

where $\int_{V_{0}}(\bullet)dV_{0}$ stands for integration over the Lagrangian volume. On the other hand

$$\begin{aligned}\delta W_{mech}&=\int_{V_{0}}\left[\phi\left(\mathbf{F}^{e}+\frac{\partial\delta\mathbf{x}}{\partial\mathbf{x}}\cdot\mathbf{F}^{e},C^{H},C^{Li},\theta,\alpha\right)-\phi(\mathbf{F}^{e},C^{H},C^{Li},\theta,\alpha)\right]dV_{0}\\&=\int_{V_{0}}\left[\left.\frac{\partial\phi}{\partial F_{jk}^{e}}\right|_{C^{H},C^{G},\theta,\alpha}\frac{\partial\delta x_{j}}{\partial x_{l}}F_{lk}^{e}\right]dV_{0}=\int_{V_{0}}\left[\left.\frac{\partial\phi}{\partial F_{jk}^{e}}\right|_{C^{H},C^{G},\theta,\alpha}\frac{\partial\delta x_{j}}{\partial X_{K}}f_{K\,k}^{SF}\right]dV_{0}.\end{aligned} \tag{8}$$

Here, $\mathbf{f}^{SF}\equiv(\mathbf{F}^{SF})^{-1}$. A comparison of (7) and (8) leads to

$$\sigma^{PK1}_{Kj}=\left.\frac{\partial\phi}{\partial F^e_{jk}}\right|_{C^H,C^G,\theta,\alpha} f^{SF}_{K\,k} \tag{9}$$

and

$$\sigma_{ij}=\frac{1}{\det(\mathbf{F})}F_{iK}\sigma^{PK1}_{Kj}=\frac{1}{\det(\mathbf{F})}F^e_{ik}\left.\frac{\partial\phi}{\partial F^e_{jk}}\right|_{C^H,C^G,\theta,\alpha}. \tag{10}$$

Following Wu (2001), the chemical potential of guest is given by

$$\mu^G=\left.\frac{\partial\phi}{\partial C^G}\right|_{\mathbf{F},C^H,\theta,\alpha}=\left.\frac{\partial\phi}{\partial F^e_{ij}}\right|_{C^H,C^G,\theta,\alpha}\left.\frac{\partial F^e_{ij}}{\partial C^G}\right|_{\mathbf{F},C^H,\theta,\alpha}+\left.\frac{\partial\phi}{\partial C^G}\right|_{\mathbf{F}^e,C^H,\theta,\alpha}. \tag{11}$$

Since $(\partial\mathbf{f}^{SF}/\partial C^G)=-\mathbf{f}^{SF}(\partial\mathbf{F}^{SF}/\partial C^G)\mathbf{f}^{SF}$

$$\left.\frac{\partial\mathbf{F}^e}{\partial C^G}\right|_{\mathbf{F},C^H,\theta,\alpha}=\left.\frac{\partial(\mathbf{F}\cdot\mathbf{f}^{SF})}{\partial C^G}\right|_{\mathbf{F},C^H,\theta,\alpha}=-\mathbf{F}^e\cdot\left.\frac{\partial\mathbf{F}^{SF}}{\partial C^G}\right|_{\mathbf{F},C^H,\theta,\alpha}\cdot\mathbf{f}^{SF}. \tag{12}$$

Substitution of Eqs. (12) into (11) leads to

$$\mu^G=\left.\frac{\partial\phi}{\partial C^G}\right|_{\mathbf{F}^e,C^H,\theta,\alpha}-\left.\frac{\partial\phi}{\partial F^e_{ij}}\right|_{C^H,C^G,\theta,\alpha}F^e_{ik}\left.\frac{\partial F^{SF}_{kl}}{\partial C^G}\right|_{\mathbf{F},C^H,\theta,\alpha}f^{SF}_{lj}. \tag{13}$$

With Eqs. (10) and (13), the guest (lithium) chemical potential can be related to the Cauchy stress by

$$\mu^G=\left.\frac{\partial\phi}{\partial C^G}\right|_{\mathbf{F}^e,C^H,\theta,\alpha}-\det(\mathbf{F})f^e_{mi}\sigma_{ij}F^e_{jk}\left.\frac{\partial F^{SF}_{kl}}{\partial C^G}\right|_{\mathbf{F},C^H,\theta,\alpha}f^{SF}_{lm}. \tag{14}$$

By the same token, the chemical potential of the host atoms can be written as

$$\mu^H=\left.\frac{\partial\phi}{\partial C^H}\right|_{\mathbf{F}^e,C^G,\theta,\alpha}-\det(\mathbf{F})f^e_{mi}\sigma_{ij}F^e_{jk}\left.\frac{\partial F^{SF}_{kl}}{\partial C^H}\right|_{\mathbf{F},C^G,\theta,\alpha}f^{SF}_{lm}. \tag{15}$$

2.4. Kinetics

According to Wu (2001), the Clausius–Duhem inequality can be stated in the Lagrangian frame as

$$\begin{aligned}&-\left[\dot\phi+\eta\dot\theta-\boldsymbol{\sigma}^{PK1}_{Ki}\dot F_{iK}-\mu^H\dot C^H-\mu^G\dot C^G\right]\\&\quad+\theta\mathbf{J}^{(q)}\cdot\nabla_{\boldsymbol{X}}\left(\frac{1}{\theta}\right)+\theta\mathbf{J}^H\cdot\nabla_{\boldsymbol{X}}\left(-\frac{\mu^H}{\theta}\right)+\theta\mathbf{J}^G\cdot\nabla_{\boldsymbol{X}}\left(-\frac{\mu^G}{\theta}\right)\ge0,\end{aligned} \tag{16}$$

where $\mathbf{J}^{(q)}$ is the heat flux measured in the Lagrangian frame and η is the Lagrangian density of entropy. Under isothermal conditions with $\dot\theta=0$ and $\nabla_{\mathbf{X}}\theta=\mathbf{0}$,

$$-\left[\dot\phi-\boldsymbol{\sigma}^{PK1}_{Ki}\dot F_{iK}-\mu^H\dot C^H-\mu^G\dot C^G\right]+\theta\mathbf{J}^H\cdot\nabla_{\boldsymbol{X}}\left(-\frac{\mu^H}{\theta}\right)+\theta\mathbf{J}^G\cdot\nabla_{\boldsymbol{X}}\left(-\frac{\mu^G}{\theta}\right)\ge0. \tag{17}$$

On the other hand, because $\dot\theta=0$

$$\dot\phi=\left.\frac{\partial\phi}{\partial F^e_{ij}}\right|_{C^H,C^G,\theta,\alpha}\dot F^e_{ij}+\left.\frac{\partial\phi}{\partial C^H}\right|_{\mathbf{F}^e,C^G,\theta,\alpha}\dot C^H+\left.\frac{\partial\phi}{\partial C^G}\right|_{\mathbf{F}^e,C^H,\theta,\alpha}\dot C^G+\left.\frac{\partial\phi}{\partial\alpha}\right|_{\mathbf{F}^e,C^H,C^G,\theta}\dot\alpha. \tag{18}$$

Since $\boldsymbol{\sigma}^{PK1}_{Ki}\dot F_{iK}=\det(\mathbf{F})\sigma_{ij}D_{ji}$, Eqs. (18), (14), (15), (10) and (2) lead to

$$\dot\phi-\boldsymbol{\sigma}^{PK1}_{Ki}\dot F_{iK}-\mu^H\dot C^H-\mu^G\dot C^G=\left.\frac{\partial\phi}{\partial\alpha}\right|_{\mathbf{F}^e,C^H,C^G,\theta}\dot\alpha+\det(\mathbf{F})f^e_{mi}\sigma_{ij}F^e_{jk}f^{SF}_{lm}\left[\left.\frac{\partial F^{SF}_{kl}}{\partial C^G}\right|_{\mathbf{F},C^H,\theta,\alpha}\dot C^G+\left.\frac{\partial F^{SF}_{kl}}{\partial C^H}\right|_{\mathbf{F},C^G,\theta,\alpha}\dot C^H\right]-\det(\mathbf{F})\sigma_{ij}D^{SF}_{ji}. \tag{19}$$

By Eqs. (19), (17) and (3), the isothermal Clausius–Duhem inequality in the updated Lagrangian frame takes the form

$$\gamma_\alpha+\mathbf{j}^G\cdot\nabla_{\mathbf{x}}(-\mu^G)+\mathbf{j}^H\cdot\nabla_{\mathbf{x}}(-\mu^H)\ge0, \tag{20}$$

where the local dissipation rate γ_α is defined as

$$\gamma_\alpha\equiv\sigma_{ij}D^{SF}_{ji}-f^e_{mi}\sigma_{ij}F^e_{jk}f^{SF}_{lm}\left[\left.\frac{\partial F^{SF}_{kl}}{\partial C^G}\right|_{\mathbf{F},C^H,\theta,\alpha}\dot C^G+\left.\frac{\partial F^{SF}_{kl}}{\partial C^H}\right|_{\mathbf{F},C^G,\theta,\alpha}\dot C^H\right]-\frac{1}{\det(\mathbf{F})}\left.\frac{\partial\phi}{\partial\alpha}\right|_{\mathbf{F}^e,C^H,C^G,\theta}\dot\alpha. \tag{21}$$

In general, the stress-free deformation F^{SF} can be a function of C^G,C^H and the internal state variable α, i.e.,

$$\mathbf{F}^{SF}=\mathbf{F}^{SF}(C^H,C^G,\alpha). \tag{22}$$

By Eq. (2)

$$\sigma_{ij}D^{SF}_{ji}=\sigma_{ij}F^e_{jk}\dot{F}^{SF}_{kl}f^{SF}_{lm}f^e_{mi}. \tag{23}$$

Therefore, Eqs. (21)–(23) combine to give

$$\begin{cases}\gamma_\alpha=f_\alpha\dot{\alpha},\\ f_\alpha\equiv f^e_{mi}\sigma_{ij}F^e_{jk}f^{SF}_{lm}\left.\frac{\partial F^{SF}_{kl}}{\partial\alpha}\right|_{\mathbf{F},C^H,C^G,\theta}-\frac{1}{\det(\mathbf{F})}\left.\frac{\partial\phi}{\partial\alpha}\right|_{\mathbf{F}^e,C^H,C^G,\theta}.\end{cases} \tag{24}$$

The kinetic driving force can be defined as

$$\mathbf{X}_{kin}\equiv\left[f_\alpha,\nabla_{\mathbf{x}}(-\mu^G),\nabla_{\mathbf{x}}(-\mu^H)\right]^T \tag{25}$$

and the associated response is

$$\mathbf{J}_{kin}\equiv[\dot{\alpha},\mathbf{j}^G,\mathbf{j}^H]^T=\mathbf{J}_{kin}(\mathbf{X}_{kin}). \tag{26}$$

The kinetic response of the electrode material is specified through the driving force–response relation $\mathbf{J}_{kin}=\mathbf{J}_{kin}(\mathbf{X}_{kin})$, which must satisfy the Clausius–Duhem inequality in the form of

$$\mathbf{J}^T_{kin}\cdot\mathbf{X}_{kin}\geq 0. \tag{27}$$

In this paper, the simplest linear "diagonal" form is chosen for Eq. (26) such that

$$\begin{cases}\dot{\alpha}=c_\alpha f_\alpha,\\ j^G_i=-\frac{D^G_{ik}}{k_B\theta}c^G\frac{\partial\mu^G}{\partial x_k}\quad and\\ j^H_i=-\frac{D^H_{ik}}{k_B\theta}c^H\frac{\partial\mu^H}{\partial x_k}.\end{cases} \tag{28}$$

In the above relations, D^G_{ik} and D^H_{ik} are the positive-definite tensorial diffusivity of guest and host, respectively; c_α is the linear coefficient for internal state variable evolution and k_B is the Boltzmann constant. The dissipation due to plastic flow is not considered here because the stresses are assumed to be below the yield threshold.

It is often convenient to evaluate the fluxes in the Lagrangian frame. These fluxes can be obtained from Eq. (28) through

$$\begin{cases}J^G_K=-\frac{D^G}{k_B\theta}f_{Ki}f_{Ji}C^G\frac{\partial\mu^G}{\partial X_J}\quad and\\ J^H_K=-\frac{D^H}{k_B\theta}f_{Ki}f_{Ji}C^H\frac{\partial\mu^H}{\partial X_J}.\end{cases} \tag{29}$$

2.5. Constitutive behaviors of fully amorphized isotropic electrode materials

Eqs. (6), (10), (14), (15), (25) and (26) provide a general framework for two-species electrode materials below plastic yield threshold. To proceed, material-specific relationships [Eqs. (6), (22) and (26)] need to be specified. Since the electrode material of interest here is fully amorphized Li-alloys, several further assumptions are in order.

2.5.1. Full amorphization

The theoretical framework in this paper is capable of phenomenologically capturing the amorphization process in the first few charging cycles. Such a process of amorphization is not considered here, mainly due to the lack of experimental data on the evolution law. Instead, the alloy is assumed to have fully amorphized, with saturated degree of amorphization, i.e. $\dot{\alpha}=0$. This assumption is reasonable because full amorphization is achieved after only a few charge–discharge cycles for an initially crystalline Si electrode. The isothermal Helmholtz free energy density thus becomes

$$\phi=\phi(\mathbf{F}^e,C^H,C^G). \tag{30}$$

2.5.2. Small elastic deformation

The elastic deformation is assumed to be small compared to the total deformation and can be characterized by the elastic strain

$$\boldsymbol{\varepsilon}^e\equiv\frac{1}{2}((\mathbf{F}^e)^T(\mathbf{F}^e)-\mathbf{I}). \tag{31}$$

The Helmholtz free energy density can therefore be written as the sum of a stress-free part and an elastic part (Wu, 2001), i.e.,

$$\phi=\phi(\mathbf{F}^e,C^H,C^G)=\phi^{SF}(C^H,C^G)+\frac{1}{2}J^{SF}C_{ijkl}\varepsilon^e_{ij}\varepsilon^e_{kl}, \tag{32}$$

where $C_{ijkl}=C_{ijkl}(C^H,C^G)$ is the elastic modulus which depends on material composition in general. $J^{SF}\equiv\det(\mathbf{F}^{SF})$ is the Jacobian of the stress-free expansion.

2.5.3. Isotropy

The physical properties of the electrode material are assumed to be isotropic. Specifically, the diffusivities are assumed to be of the forms

$$\left.\begin{array}{l} D^G_{ik}=D^G\delta_{ik} \quad and \\ D^{Si}_{ik}=D^{Si}\delta_{ik}, \end{array}\right\} \tag{33}$$

the stress-free expansion is

$$\mathbf{F}^{SF}=[J^{SF}(C^H,C^G)]^{1/3}\mathbf{I}, \tag{34}$$

and the elastic response is also assumed to be isotropic such that

$$\phi=\phi(\mathbf{F}^e,C^H,C^G)=\phi^{SF}(C^H,C^G)+J^{SF}\left[\frac{9}{2}K\varepsilon^{e2}_m+G\varepsilon^{e\prime}_{ij}\varepsilon^{e\prime}_{ij}\right]. \tag{35}$$

Here, $\varepsilon^e_m\equiv\varepsilon^e_{kk}/3$ and $\varepsilon^{e\prime}_{ij}\equiv\varepsilon^e_{ij}-\varepsilon^e_m\delta_{ij}$ are, respectively, the isotropic and deviatoric parts of the elastic strain; K and G are the composition-dependent bulk and shear modulus, respectively. Eqs. (10) and (35) lead to

$$\sigma_{ij}=F^e_{iK}(3K\varepsilon^e_m\delta_{KL}+2G\varepsilon^{e\prime}_{KL})F^e_{jL}, \tag{36}$$

where second-order terms of $\boldsymbol{\varepsilon}^e$ have been neglected due to the assumption of small elastic deformation. The particular form of Eq. (36) ensures that the correct rotational relationship between $\boldsymbol{\varepsilon}^e$ and $\boldsymbol{\sigma}$ is maintained. With Eqs. (14), (15), (35) and (36), the chemical potential of the host and guest can be shown to be

$$\left\{\begin{array}{l} \mu^H=\left.\dfrac{\partial\phi^{SF}}{\partial C^H}\right|_{\boldsymbol{\varepsilon}^e=\mathbf{0},C^G}-\dfrac{1}{3}\det(\mathbf{F}^e)\Omega^{H(SF)}\sigma_{kk} \quad and \\ \mu^G=\left.\dfrac{\partial\phi^{SF}}{\partial C^G}\right|_{\boldsymbol{\varepsilon}^e=\mathbf{0},C^H}-\dfrac{1}{3}\det(\mathbf{F}^e)\Omega^{G(SF)}\sigma_{kk}; \end{array}\right. \tag{37}$$

where $\Omega^{H(SF)}\equiv\partial J^{SF}/\partial C^H\big|_{C^G}$ and $\Omega^{G(SF)}\equiv\partial J^{SF}/\partial C^G\big|_{C^H}$ are the stress-free partial atomic volume of the host and guest, respectively. Again, second-order terms of $\boldsymbol{\varepsilon}^e$ are neglected in the derivation of Eq. (37). It should be pointed out that under the condition that $\boldsymbol{\varepsilon}^e=0$ and $\boldsymbol{\sigma}=0$, the stress-free Helmholtz free energy density $\phi^{SF}\big|_{\boldsymbol{\varepsilon}^e=\mathbf{0}}$ is equal to the stress-free Gibbs free energy density $\psi^{SF}|_{\boldsymbol{\sigma}=0}$ because the Legendre transformation term is zero. Therefore, Eq. (37) can also take the form of

$$\left\{\begin{array}{l} \mu^H=\left.\dfrac{\partial\psi^{SF}}{\partial C^H}\right|_{\boldsymbol{\sigma}=\mathbf{0},C^G}-\dfrac{1}{3}\det(\mathbf{F}^e)\Omega^{H(SF)}\sigma_{kk}=\mu^H_*+k_B\theta\ln\gamma^Hx^H-\det(\mathbf{F}^e)\Omega^{H(SF)}\sigma_m \quad and \\ \mu^G=\left.\dfrac{\partial\psi^{SF}}{\partial C^G}\right|_{\boldsymbol{\sigma}=\mathbf{0},C^H}-\dfrac{1}{3}\det(\mathbf{F}^e)\Omega^{G(SF)}\sigma_{kk}=\mu^G_*+k_B\theta\ln\gamma^Gx^G-\det(\mathbf{F}^e)\Omega^{G(SF)}\sigma_m, \end{array}\right. \tag{38}$$

where μ^H_* and μ^G_* are the reference-state chemical potentials; and γ^H and γ^G are the stress-free activity coefficients. $\sigma_m\equiv\sigma_{kk}/3$ is the hydrostatic stress.

Finally, substituting Eqs. (38) into (29) and neglecting second-order terms of $\boldsymbol{\varepsilon}^e$ lead to

$$\left\{\begin{array}{l} J^H_K=-D^Hf_{Ki}f_{Ji}\Phi\cdot\left(x^G\dfrac{\partial C^H}{\partial X_J}-x^H\dfrac{\partial C^G}{\partial X_J}\right)+\dfrac{D^H}{k_B\theta}f_{Ki}f_{Ji}C^H\dfrac{\partial[\Omega^{H(SF)}\sigma_m]}{\partial X_J} \quad and \\ J^G_K=-D^Gf_{Ki}f_{Ji}\Phi\cdot\left(x^H\dfrac{\partial C^G}{\partial X_J}-x^G\dfrac{\partial C^H}{\partial X_J}\right)+\dfrac{D^G}{k_B\theta}f_{Ki}f_{Ji}C^{Li}\dfrac{\partial[\Omega^{G(SF)}\sigma_m]}{\partial X_J}, \end{array}\right. \tag{39}$$

where $\Phi\equiv1+(x^G/\gamma^G)(\partial\gamma^G/\partial x^G)=1+(x^H/\gamma^H)(\partial\gamma^H/\partial x^H)$ is the stress-free thermodynamic factor which is assumed to depend only on the composition x^G or x^H.

3. Numerical formulation with mixed finite elements

In Eq. (39), the diffusion fluxes of the host and guest consist of two parts each. The stress-free (chemical) parts

$$\begin{cases} J_K^{H,chem} = -D^H f_{Ki} f_{Ji} \Phi \cdot \left(x^G \dfrac{\partial C^H}{\partial X_J} - x^H \dfrac{\partial C^G}{\partial X_J} \right) & and \\ J_K^{G,chem} = -D^G f_{Ki} f_{Ji} \Phi \cdot \left(x^H \dfrac{\partial C^G}{\partial X_J} - x^G \dfrac{\partial C^H}{\partial X_J} \right) \end{cases} \tag{40}$$

are due to chemical interactions between the guest and host atoms. The mechanical parts

$$\begin{cases} J_K^{H,mech} = \dfrac{D^H}{k_B \theta} f_{Ki} f_{Ji} C^H \dfrac{\partial [\Omega^{H(SF)} \sigma_m]}{\partial X_J} & and \\ J_K^{G,mech} = \dfrac{D^G}{k_B \theta} f_{Ki} f_{Ji} C^G \dfrac{\partial [\Omega^{G(SF)} \sigma_m]}{\partial X_J} \end{cases} \tag{41}$$

are due to stresses which tend to squeeze the atoms from compressive regions to tensile regions. It has been suggested that the stress-induced contributions may significantly affect concentrations and stresses in Li-ion battery electrodes (Zhang et al., 2007; Zhao et al., 2011a, 2011b). For nanowire electrodes made of Li/Si, the stress effect could amount to a 303% increase in the effective diffusivity, thereby significantly decrease the stress levels (Gao and Zhou, 2011). Therefore, $J_K^{H,mech}$ and $J_K^{G,mech}$ must be captured to correctly evaluate the stress levels and assess resulting failure in Li-alloy electrodes.

One of the major numerical challenges here is associated with the gradient of hydrostatic stress (i.e. $\partial\sigma_m/\partial X_J$) that appears in Eq. (41) when a finite element (FE) method is used. Since $\partial\sigma_m/\partial X_J \propto \partial\varepsilon_m^e/\partial X_J$, either the strain gradient or the stress gradient itself has to be calculated numerically. Tang et al. (2010a) used a finite difference method to calculate the diffusion–stress coupling in olivine electrodes and successfully reproduced the phase transformation characteristics observed in experiments. The benefit of using a finite difference scheme is that one automatically captures the second-order deformation gradient by using appropriate discretized gradient operators. The finite element method, however, is more valuable if geometric shapes other than rectangles are involved.

When a linear interpolation is used with a finite element, the information of strain gradient is lost since the diagonal terms of the interpolator's spatial Hessian are always zero. One remedy is to use elements with high-order polynomials as the interpolation functions. Another strategy is to compute the second-order deformation gradients by fitting to nodal displacements across several adjacent elements, instead of relying only on the nodal values of one specific element under consideration (Abu Al-Rub and Voyiadjis, 2005). These methods fall into the category of irreducible finite element methods.

Here, we propose a mixed form finite element framework to simulate the diffusion/deformation coupling. Instead of using only the deformation and host/guest concentrations as the nodal variables, we interpolate σ_m as a redundant degree of freedom, thereby automatically resolve $\partial\sigma_m/\partial X_J$ required in Eq. (41). Section 3 is devoted to the mixed FE scheme and the numerical results of interdiffusion/deformation coupling are left to Section 4.

3.1. Variational form

The mixed FE method was originally proposed to avoid numerical singularity in problems of incompressible solids, for which the hydrostatic stress σ_m cannot be well-defined in terms of the displacement field. As a remedy, the hydrostatic stress can be introduced as a Lagrangian multiplier to enforce the incompressibility, hence the name "mixed" finite element. Similar concepts were later adopted to capture the strain gradient effects in non-local theories of plasticity by treating either the rotation or the full deformation gradient as redundant variables (Luscher et al., 2010; Shu et al., 1999). Mixed FE methods have also been used in soil mechanics, in which transport of incompressible fluid in porous media is mainly driven by pressure gradients (Borja et al., 1998). Although the concept of mixed FE could be very useful to calculate $\partial\sigma_m/\partial X_J$ in Eq. (41), we are not aware of any work that uses it for diffusion/deformation coupling problems in battery electrodes. Here, we treat the hydrostatic stress $\sigma_m(X,t)$ as though it was an independent field variable in order to facilitate the calculation of its gradients. We call σ_m a redundant variable, in contrast to truly independent field variables such as $\mathbf{u}(\mathbf{X},t)=\mathbf{x}-\mathbf{X}$, C^H and C^G. This redundant variable is implicitly constrained by Eq. (36), i.e.,

$$3\varepsilon_m^e - \sigma_m/K = 0. \tag{42}$$

Here, second-order terms of $\boldsymbol{\varepsilon}^e$ are neglected in the derivation of Eq. (42). Since $\det(\mathbf{F}) = \det(\mathbf{F}^e)\det(\mathbf{F}^{SF}) = \det(\mathbf{F}^e)J^{SF}$ and $\varepsilon_m^e \approx (\det(\mathbf{F}^e)-1)/3$, the constraint condition in (42) can be restated in the variational form of

$$\int_V \left[\frac{\det(\mathbf{F})}{J^{SF}(C^H, C^G)} - 1 - \frac{\sigma_m}{K} \right] \delta\sigma_m dV = 0, \tag{43}$$

where $\int_V(\bullet)dV$ stands for integration over the current configuration of the body. The same constraint in the Lagrangain domain V_0 is

$$\int_{V_0} \det(\mathbf{F}) \left[\det(\mathbf{F})/J^{SF} - 1 - \sigma_m/K \right] \delta\sigma_m \, dV_0 = 0 \tag{44}$$

The variational statement of the conservation of momentum [Eq. (5)], on the other hand, takes the standard form

$$\int_{V_0} \sigma_{Ji}^{PK1} \frac{\partial \delta u_i}{\partial X_J} dV_0 = \int_{S_0} T_i \delta u_i \, dS_0 + \int_{V_0} B_i \cdot \delta u_i \, dV_0, \tag{45}$$

where $\sigma_{Ji}^{PK1} = \det(\mathbf{F}) f_{Jj} \sigma_{ji}$ and

$$\sigma_{ij} = \sigma_m \delta_{ij} + 2G F_{iK}^e \varepsilon_{KL}^{e\prime} F_{jL}^e. \tag{46}$$

Here, σ_m is treated as an independent variable. $\int_{S_0}(\bullet) dS_0$ stands for integration over the surface of the Lagrangian domain. T and B are the surface traction and body forces in the Lagrangian frame, respectively.

Finally, the conservation of mass [Eq. (4)] requires

$$\int_{V_0} \left. \frac{\partial C^S}{\partial t} \right|_{\mathbf{X}} \cdot \delta C^S \, dV_0 = \int_{V_0} J_K^S \frac{\partial \delta C^S}{\partial X_K} dV_0 + \int_{V_0} R_b^S \delta C^S \, dV_0 + \int_{S_0} Q^S \delta C^S \, dS_0 \quad (S = G, \ H), \tag{47}$$

where Q^G and Q^H are the Lagrangian surface influxes. The fluxes J_K^G and J_K^H are given by Eq. (39), with σ_m being treated as an independent variable.

3.2. Discretization

The variational forms in Eqs. (43)–(47) are discretized using the FE interpolations of

$$\begin{cases} \mathbf{x}(\mathbf{X},t) = \sum_a N_a^{\mathbf{x}}(\mathbf{X}) \mathbf{x}_a(t), \\ C^G(\mathbf{X},t) = \sum_a N_a^C(\mathbf{X}) C_a^G(t), \\ C^H(\mathbf{X},t) = \sum_a N_a^C(\mathbf{X}) C_a^H(t) \quad \textit{and} \\ \sigma_m(\mathbf{X},t) = \sum_a N_a^{\sigma_m}(\mathbf{X}) \sigma_m^a(t), \end{cases} \tag{48}$$

where $N_a^{\mathbf{x}}(\mathbf{X})$, $N_a^C(\mathbf{X})$ and $N_a^{\sigma_m}(\mathbf{X})$ are shape functions for the displacement, concentration and hydrostatic stress degrees of freedom (DOF), respectively; $\mathbf{x}_a(t)$, $C_a^G(t)$, $C_a^H(t)$ and $\sigma_m^a(t)$ are the corresponding time-dependent nodal values. Here, second-order isoparametric shape functions are used for $N_a^{\mathbf{x}}(\mathbf{X})$ and linear isoparametric shape functions are chosen for $N_a^C(\mathbf{X})$ and $N_a^{\sigma_m}(\mathbf{X})$ [cf. Fig. 2]. This interpolation scheme gives sufficient accuracy for the $\partial\sigma_m/\partial X_J$ effect in Eq. (41) yet does not introduce too many redundant DOF which may result in singular Jacobian matrices (Zienkiewicz and Taylor, 2000).

Substitution of Eq. (48) into (45) leads to

$$\sum_a \left[-\int_{V_0} \sigma_{Ji}^{PK1} \frac{\partial N_a^{\mathbf{x}}}{\partial X_J} dV_0 + \int_{S_0} T_i \cdot N_a^{\mathbf{x}} \, dS_0 + \int_{V_0} B_i \cdot N_a^{\mathbf{x}} \, dV_0 \right] \delta u_{ai} = 0. \tag{49}$$

The nodal force which is work-conjugate to δu_{ai} is, therefore,

$$F_{u_{ai}}(t) \equiv -\int_{V_0} \sigma_{Ji}^{PK1} \frac{\partial N_a^{\mathbf{x}}}{\partial X_J} dV_0 + \int_{S_0} T_i \cdot N_a^{\mathbf{x}} \, dS_0 + \int_{V_0} B_i \cdot N_a^{\mathbf{x}} \, dV_0, \tag{50}$$

where the stress is given by Eq. (46). By the same token, the residual associated with the $\delta C_a^S (S = G,H)$ DOF is

$$F_{C_a^S}(t) \equiv -\sum_b \kappa_{ab} \dot{C}_b^S + \int_{V_0} J_K^S \frac{\partial N_a^C}{\partial X_K} \, dV_0 + \int_{V_0} R_b^S N_a^C dV_0 + \int_{S_0} Q^S N_a^C \, dS_0, \ (S = G,H), \tag{51}$$

where $\kappa_{ab} \equiv \int_{V_0} N_a^C N_b^C \, dV_0$ is the consistent capacity matrix.

Finally, substitution of Eq. (48) into the constraint condition in Eq. (44) yields the requirement

$$\sum_a \left\{ \int_{V_0} \det(\mathbf{F}) [\det(\mathbf{F})/J^{SF} - 1 - \sigma_m/K] N_a^{\sigma_m}(\mathbf{X}) \, dV_0 \delta \sigma_m^a \right\} = 0. \tag{52}$$

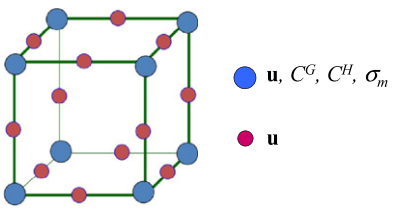

Fig. 2. The mixed finite element used to calculate deformation/interdiffusion coupling in alloy-based electrodes. Second-order isoparametric shape functions are used for displacement and linear isoparametric shape functions are used for concentration and pressure. The corner nodes have displacement, concentration and hydrostatic stress DOF and the edge nodes only have displacement DOF.

The residual associated with the $\delta\sigma_m^a$ DOF is, therefore,

$$F_{\sigma_m^a}(t) \equiv -\int_{V_0} \det(\mathbf{F})[\det(\mathbf{F})/J^{SF} - 1 - \sigma_m/K]N_a^{\sigma_m}\, dV_0. \tag{53}$$

Now, the deformation/diffusion coupling problem had been reduced to a set of nonlinear ODEs that must be satisfied for all nodes

$$F_{u_{ai}}(t) = 0, \quad F_{\sigma_m^a}(t) = 0, \quad F_{C_a^S}(t) = 0. \tag{54}$$

The first two equations in (54) are simply non-linear algebraic equations. To solve the third, we need to further discretize the time variable. For increment (t_n, t_{n+1}), we use the unconditionally stable backward Euler integration scheme, i.e.,

$$F_{C_a^S}(t_{n+1}) \approx -\sum_b \kappa_{ab} \frac{C_b^S(t_{n+1}) - C_b^S(t_n)}{\Delta t_{n+1}} + \int_{V_0} J_K^S(t_{n+1}) \frac{\partial N_a^C}{\partial X_K} dV_0 + \int_{V_0} R_b^S(t_{n+1}) N_a^C\, dV_0 + \int_{S_0} Q^S(t_{n+1}) N_a^C\, dS_0 \quad (S = G, H), \tag{55}$$

where $\Delta t_{n+1} \equiv t_{n+1} - t_n$ is the time increment of interval (t_n, t_{n+1}). The diffusion fluxes J_K^S, body source/sink R_b^S and surface influx Q^S should be evaluated at the end of (t_n, t_{n+1}), as indicated by Eq. (55). The first two equations in (54), on the other hand, can be discretized by simply evaluating Eqs. (50) and (53) at time t_{n+1}, i.e.,

$$\begin{cases} F_{u_{ai}}(t_{n+1}) = 0 \quad \textit{and} \\ F_{\sigma_m^a}(t_{n+1}) = 0. \end{cases} \tag{56}$$

The 3D mixed finite element framework is implemented using the UEL interface of ABAQUS Standard 6.10. Gaussian quadrature is used to integrate the residuals, with 27 integration points for $F_{u_{ai}}$ and eight integration points for $F_{C_a^S}$ and $F_{\sigma_m^a}$. Since the well-know Newtown iteration method is used by ABAQUS to solve the non-linear algebraic equations in (55) and (56), Jacobians of $F_{u_{ai}}$, $F_{C_a^S}$ and $F_{\sigma_m^a}$ with respect to nodal variables at t_{n+1} are needed. The derivation of these Jacobians is standard and is not elaborated here.

4. Stress relaxation in Li/Si nanowire electrodes due to host diffusion

The electric and mechanical properties of Li/Si alloy are highly dependent on the lithium concentration and state of amorphization (Kim et al., 2010, 2011; Shenoy et al., 2010). Although crystalline silicon is highly brittle, nano-sized Li/Si alloy can be highly ductile (Hertzberg et al., 2011). This ductility is desirable since it relieves stresses and reduces the possibility of crack development (Zhao et al., 2011a). Characteristics of the diffusion kinetics, especially the diffusivities, in Li/Si has also been studied extensively (Ding et al., 2009; Pell, 1960; Ruffo et al., 2009; Xie et al., 2010). In particular, first principle calculations indicate that the mobility of silicon in Li/Si can be non-negligible, with the diffusivity ratio D^{Si}/D^{Li} being $\sim$0.5 at 1050 K (Kim et al., 2011). Very recently, Johari et al. (2011) calculated the diffusivity of both Li and Si in silicon-based electrodes at room temperature and found that the diffusivity ratio in a-Si falls into the range of $D^{Si}/D^{Li} = 0.8\times10^{-2}$–$1.39\times10^{-2}$. As will be demonstrated by the mixed FE calculations later in this paper, even such low D^{Si}/D^{Li} values have significant impact on the evolution of stresses, primarily because of the chemical interactions between the species and the effect of stress gradient on interdiffusion. It should be noted that the study by Johari et al. was conducted on Li/Si systems with the composition of $Li_{1.0}Si$. For higher x^{Li}, D^{Si}/D^{Li} could be even higher since more Si–Si covalent bonds are weakened or broken.

Here we analyze the implication of a small but non-zero D^{Si} in amorphous Li/Si electrodes (host H=Si and guest G=Li) using the mixed FE method developed. One focus of the analysis is the relative importance of the mechanical driving force [Eq. (41)] and the chemical driving force [Eq. (40)] for host atom migration.

4.1. Migration of host atoms in Li/Si nanowire electrodes

We consider a cylindrical Li/Si nanowire [inset of Fig. 3(a)] with radius ρ_0=250 nm when fully discharged. This fully-discharged state is taken to be the Lagrangian reference state. The NW is charged from its outer cylindrical surface at a constant Lagrangian lithium influx Q^{Li} [cf. Eq. (47)]. Under galvanostatic conditions,

$$Q^{Li} = \frac{1}{2}\rho_0 C_0^{Si} \xi_{\max} \frac{1}{T_0}, \tag{57}$$

where $\xi_{\max} = 4.4$ is the maximum charging limit for lithium per silicon, C_0^{Si}=49.3 atoms/nm^3 is the silicon concentration in fully discharged state (the density of pure amorphous Si is 2.30 g/cm^3) (Szabadi et al., 1998), and T_0 is the nominal time required to attain full charge. In this paper, we take T_0=1 h (i.e. at 1C charging rate). End effects are neglected because the aspect ratio of the NW is assumed to be very large. Numerically, this is achieved by forcing the top and bottom surfaces to remain flat using the multi-point constraint (MPC) functionality in ABAQUS.

A linear composition–expansion curve ($\xi = x^{Li}/x^{Si}$ vs. J^{SF} curve under fixed C^{Si}) with constant partial atomic volumes $\Omega^{Si(SF)} = 1/C_0^{Si}$=20.3 Å^3 and $\Omega^{Li\ (SF)}$=14.3 Å^3 (Beaulieu et al., 2003; Gao and Zhou, 2011) is used. Recent calculations by Huang and Zhu indicates that the $\xi \sim J^{SF}$ relationship could be non-linear (Huang and Zhu, 2011). Here, a linear $\xi \sim J^{SF}$

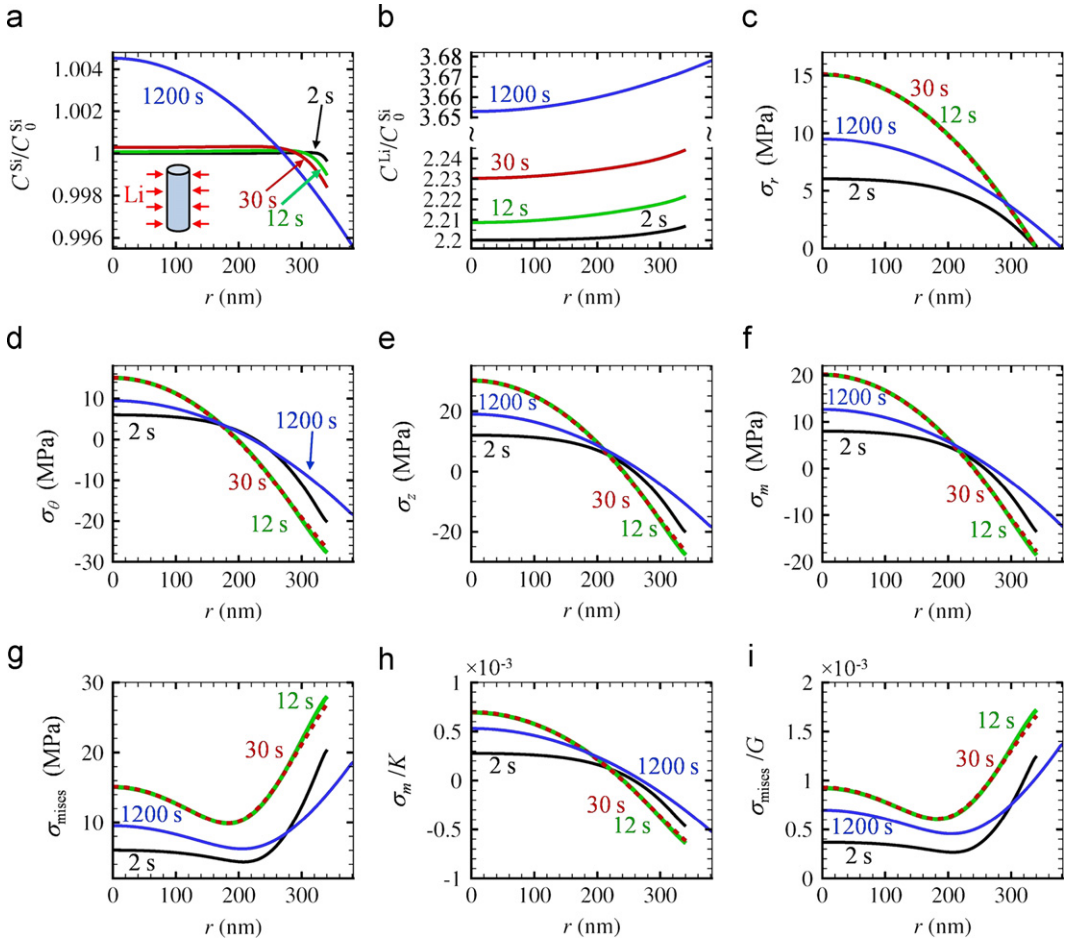

Fig. 3. Concentration and stress profiles for a Li/Si NW with radius ρ_0=250 nm, thermodynamic factor Φ=10 and diffusivity ratio D^{Si}/D^{Li}=0.02. The charging rate is 1C and the initial composition is $Li_{2.2}Si$. (a) Normalized Lagrangian silicon concentration profiles at different stages of charging, the normalization is relative to C_0^{Si}. The radial coordinate r is measured in the current configuration. The inset shows the NW charged under galvanostatic conditions at a constant surface influx Q^{Li}. The z-axis of the cylindrical coordinate system is along the NW axis. (b) Profiles of normalized Lagrangian Li concentration, the normalization is relative to C_0^{Si}. (c–g) Profiles of radial, hoop and azimuthal stress components and the hydrostatic and von Mises invariants. (h–i) Hydrostatic and von Mises stresses normalized by the composition-dependent elastic modulus (Sethuraman et al., 2010).

relation is used in order to simplify the formulation and interpretation of numerical results and to focus on the implications of non-zero host diffusivity. The concentration-dependent elastic properties are $K=K(\xi)=(12.46\xi+65.44)/(1+\xi)$ GPa and $G=G(\xi)=(7.63\xi+35.51)/(1+\xi)$ GPa (Shenoy et al., 2010). Reported D^{Li} values in Li/Si typically range from 10^{-14} to 10^{-8} $cm^2\,s^{-1}$ (Ding et al., 2009; Johari et al., 2011; Pell, 1960; Ruffo et al., 2009; Xie et al., 2010). Here, we take $D^{Li}=10^{-12}$ $cm^2\,s^{-1}$. Although the predicted stress levels depend on the value of D^{Li} according to the scaling law of $\sigma\propto 1/D^{Li}$ (Christensen and Newman, 2006), the key issue in this paper, i.e., the effect of host diffusion, is not controlled by D^{Li} itself but by the diffusivity ratio D^{Si}/D^{Li}. This host-to-guest diffusivity ratio in amorphous Si electrodes at room-temperature is found by Johari et al. (2011) to be $D^{Si}/D^{Li}=0.8\times10^{-2}$–$1.39\times10^{-2}$ for $Li_{1.0}Si$. Since silicon–silicon bonding is much weaker in high-x^{Li} states (Kim et al., 2011), D^{Si} could be even larger at higher x^{Li}. Indeed, at very low x^{Li}, D^{Si} approaches the silicon self-diffusivity which is negligible compared to D^{Li}. We therefore start our simulation at the half charged state of $Li_{2.2}Si$ in order to more realistically capture the effect of Si migration. Specifically, at $t=0$ the NW is assumed to be a homogeneously half-charged alloy with $C^{Si}_{t=0}=C^{Si}_0$ and $C^{Li}_{t=0}/C^{Si}_{t=0}=2.2$. It should be noted that the Lagrangian reference state (upon which C^{Li} and C^{Si} are measured) here is taken to be the fully discharged configuration instead of the half-charged configuration at $t=0$. A parametric study is carried out by systematically varying the D^{Si}/D^{Li} ratio from 0.005 to 0.05 while keeping $D^{Li}=10^{-12}$ $cm^2\,s^{-1}$ constant.

It should be noted that the diffusivities (D^{Li} and D^{Si}) might depend on the local stress state. Haftbaradaran et al. (2010) considered the activation barrier shift ΔE_b for lithium diffusion due to stresses (Aziz et al., 1991) and showed that the stress effect could slow down lithium diffusion through $D^{Li}=D_0^{Li}\exp(-\Delta E_b/k_B\theta)$. While stress-induced activation barrier change ΔE_b is more important under very high stresses, stress development and diffusion mainly couple through the chemical potential for moderate stresses (Yu and Suo, 2000). For Li diffusion in silicon, it has been shown that $|\Delta E_b/k_B\theta|\approx 1$ only when $|\sigma_b|$ reaches as

high as 1 GPa, otherwise, the factor $\exp(-\Delta E_b/k_B\theta)$ is negligible (Gao and Zhou, 2011). For simplicity, the effect of the factor $\exp(-\Delta E_b/k_B\theta)$ is not considered in this paper. This approximation should be valid at least for the stress levels considered in this paper.

Fig. 3(a) and (b) shows the profiles of the normalized Lagrangian concentrations $C^{Si}(r,t)/C_0^{Si}$ and $C^{Li}(r,t)/C_0^{Si}$ for a NW with $\rho_0=250$ nm, $\Phi=10$ and $D^{Si}/D^{Li}=0.02$. The Li concentration $C^{Li}(r,t)$ quickly (in less than $\sim$12 s) reaches a profile corresponding to the so-called long-term solution obtained by Gao and Zhou (2011), i.e., for most of the charging process (times beyond $\sim$12 s), the distribution of $C^{Li}(r,t)$ effectively increases uniformly over the entire wire radius, with the shape of the profiles largely unchanged. This observation is consistent with the stress profiles in Fig. 3(c–g) which show that the stress distributions for 12 s and 30 s essentially match. It should be pointed out that, strictly speaking, the shape of $C^{Li}(r,t)$ profiles does evolve even after 12 s, and the stresses at 1200 s is lower than those at 12 s and 30 s. However, this slow modulation of $C^{Li}(r,t)$ is due to composition-induced material softening (dependence of K and G on Li/Si composition), change of NW size, and Si migration, but not due to the transience of the Li diffusion process. The characteristic time τ^{Li} for reaching the steady-state gradient of $C^{Li}(r,t)$ is very short compared with the overall charging time and can be estimated to be $\tau^{Li}\approx\rho^2/\lambda_1^2 D_{eff}^{Li}$ according to the analytical solution for the case of $D^{Si}=0$ (Gao and Zhou, 2011). Here, $\rho\approx[J^{SF}(C_{t=0}^{Si},C_{t=0}^{Li})]^{1/3}\rho_0$ is approximately the NW radius during the initial stage of charging, $\lambda_1=3.8317$ is the first root of the first-order Bessel function, and

$$D_{eff}^{Li}=D^{Li}\left[\frac{\Phi}{1+C_{t=0}^{Li}/C_{t=0}^{Si}}+\frac{1}{k_B\theta}\frac{2E(\Omega^{Li(SF)})^2}{9(1-\nu)}\frac{C_{t=0}^{Li}}{J^{SF}(C_{t=0}^{Si},C_{t=0}^{Li})}\right] \tag{58}$$

is the effective diffusivity of Li. In the above relation, E and ν are Young's modulus and the Poisson ratio, respectively. For $\Phi=10$, $D^{Si}=0$ and $D^{Li}=10^{-12}$ cm^2 s^{-1}, $\tau^{Li}\approx 2.7$ s; hence long-term profiles with a steady-state shape can be expected for $C^{Li}(r,t)$ when $t>2\tau^{Li}\approx 5.4$ s (Gao and Zhou, 2011), consistent with what is seen in Fig. 3.

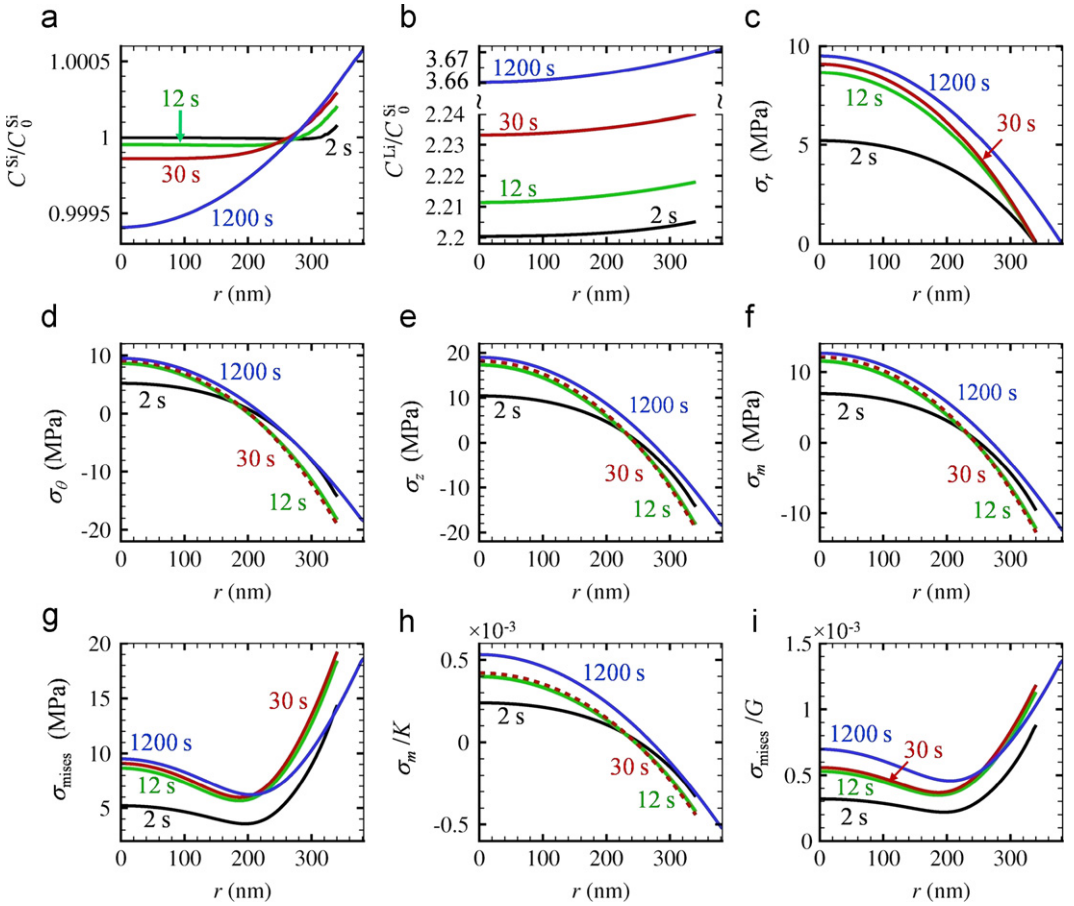

Fig. 4. Concentration and stress profiles for a NW with radius $\rho_0=250$ nm, thermodynamic factor $\Phi=90$ and diffusivity ratio $D^{Si}/D^{Li}=0.02$. The NW radius, rate of charge (1C) and an initial composition ($Li_{2.2}Si$) are the same as those in Fig. 3. (a) and (b) Normalized Lagrangian concentration profiles of silicon and lithium, respectively. (c–g) Profiles of radial, hoop, azimuthal, hydrostatic and von Mises stresses. (h–i) Hydrostatic and von Mises stresses normalized by the composition-dependent elastic bulk and shear modulus.

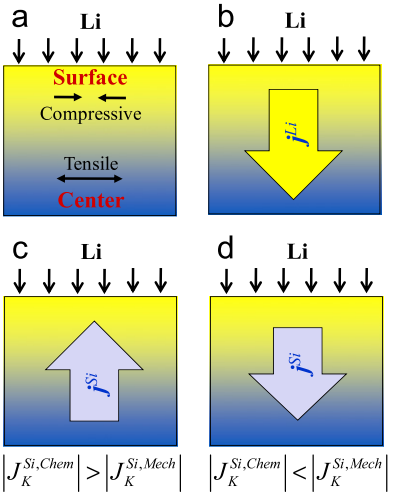

Fig. 5. The competition between the effects of chemical mixing and mechanical stress on the diffusive migration of host (Si) in Li/Si. (a) When lithium is inserted from the surface, compressive stresses develop near the surface and tensile stresses develop at the center. (b) Lithium diffuses from surface to center. (c) When the chemical effect dominates, the flow of the host (Si) is from the center to the surface of the NW. (d) When the mechanical effect dominates, the flow of the host (Si) is from the surface to the center. Realistic scenarios for Li/Si almost certainly entail (d).

The transient evolution of $C^{Si}(r,t)$ [Fig. 3(a)], on the other hand, is much slower than the transient evolution of $C^{Li}(r,t)$. As the charge progresses, C^{Si} at the NW surface decreases from the initial value and C^{Si} at the center increases from the initial value. This indicates that Si atoms slowly migrate from the surface towards the center. Like C^{Li}, C^{Si} also evolves towards a long-term steady-state profile, except that the time required by this transient evolution is longer than that for C^{Li} ($\sim$12 s), as confirmed by the $D^{Si}/D^{Li}=0.02$ curve in Fig. 6(a). The shape of the steady C^{Si} profile is shown by the curve for $t=1200$ s in Fig. 3(a). During the initial charging stage ($t<12$ s), the stresses increase and the development is similar to that for the case with $D^{Si}=0$ (Gao and Zhou, 2011). After the initial stage ($t>12$ s), the stresses slowly decrease. As seen in Fig. 3(c–g), all three stress components (radial σ_r, hoop σ_θ and longitudinal σ_z) and the two stress invariants (hydrostatic stress σ_m and the Mises equivalent stress σ_{mises}) are lower at $t=1200$ s than at $t=12$ s. One reason for the decrease in stresses is composition-change-induced softening of Li/Si alloy. Specifically, the lower elastic modulus (K and G) values at higher x^{Li} levels cause the stresses to be lower. Nonetheless, this trend remains even if the stresses are normalized by the composition-dependent bulk and shear modulus, as σ_m/K and σ_{mises}/G are still significantly lower at $t=1200$ s than at $t=12$ s [Fig. 3(h) and (i)]. This decrease of σ_m/K and σ_{mises}/G is caused by the diffusive migration of the host (Si) atoms. Since Si migrates from the surface to the center, J^{SF} increases at the center and decreases at the surface relative to the case with $D^{Si}=0$, leading to lower levels of $\boldsymbol{\varepsilon}^e$ and, consequently, the relaxation of the stresses.

To analyze the effect of the thermodynamic factor Φ, the results of a case with $\Phi=90$ and $D^{Si}/D^{Li}=0.02$ are shown in Fig. 4. The NW diameter, charging rate and diffusivities are the same as those in Fig. 3. The profiles of C^{Li} [Fig. 4(b)] and the stress components [Fig. 4(c–i)] are qualitatively similar to those for the $\Phi=10$ case in Fig. 3 for $t<30$ s, primarily because Si diffusion is too slow to have a significant influence during the initial stage, although the magnitudes of these quantities are understandably different as the effective diffusivities are dependent on Φ. The profiles of C^{Si}, however, are distinctively different. In Fig. 4, C^{Si} increases at the surface and decreases at the center; indicating Si migration is from the center to the surface. This is directly opposite to what is seen in Fig. 3. The opposite directions of Si migration lead to significant differences in the stress distributions in the NW. Specifically, at the higher thermodynamic factor value of $\Phi=90$ (higher tendency to chemically mix between the two species), the stresses at $t=1200$ s are higher than the stresses at $t=12$ s and $t=30$ s [Fig. 4(c–g)]. In contrast, at the lower thermodynamic factor value of $\Phi=10$, the stresses at $t=1200$ s are lower than the stresses at $t=12$ s and $t=30$ s. The same observations are made for the normalized stresses σ_m/K and σ_{mises}/G [Fig. 4(h–i)] as well.

The migration of Si is different between the $\Phi=10$ and $\Phi=90$ cases due to the competition between the chemical contribution [Eq. (40)] and the mechanical contribution [Eq. (41)] to the diffusive flux of silicon. The chemical contribution $\mathbf{J}^{Si,chem} \propto -\partial x^{Si}/\partial \mathbf{X}$ drives Si flow from high x^{Si} regions (center) towards low x^{Si} regions (surface), causing the composition field to homogenize. The mechanical contribution $\mathbf{J}^{Si,mech}$, on the other hand, is proportional to $\partial\sigma_m/\partial X$ and, therefore, drives Si flow from compressive regions (surface) towards the stretched regions (center). The magnitude of $\mathbf{J}^{Si,chem}$ is proportional to Φ while the magnitude of $\mathbf{J}^{Si,mech}$ is controlled by $\Omega^{Si\ (SF)}$. For $\Phi=90$, $|\mathbf{J}^{Si,chem}| > |\mathbf{J}^{Si,mech}|$ and $\mathbf{J}^{Si}=\mathbf{J}^{Si,chem}+\mathbf{J}^{Si,mech}$ points towards the surface. For $\Phi=10$, $|\mathbf{J}^{Si,chem}| < |\mathbf{J}^{Si,mech}|$ and $\mathbf{J}^{Si}$ points towards the center. This competition between the chemical effect and the mechanical effect is illustrated in Fig. 5. Here, the value of Φ can be estimated from the open-circuit potential $U^{OCP}=U^{OCP}(x^{Li})$ data via (Gao and Zhou, 2011)

$$\Phi = -(e/k_B\theta)x^{Li}dU^{OCP}/dx^{Li}. \tag{59}$$

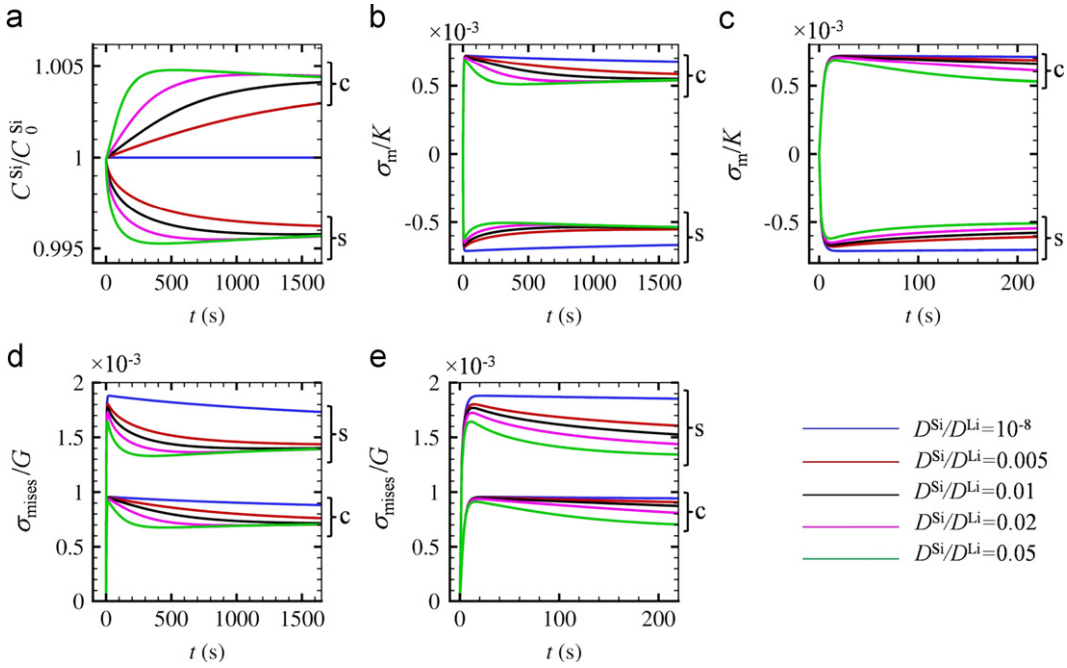

Fig. 6. Evolution of silicon concentration and stress invariants at the NW center (denoted by c) and surface (denoted by s). The NW configuration, charging rate, and thermodynamic factor Φ are the same as those in Fig. 3. The only difference is in D^{Si}/D^{Li} which is varied here. (a) Lagrangian silicon concentration normalized by C_0^{Si}. (b) Hydrostatic stress normalized by bulk modulus K; (c) details of (b) in the first 200 s. (d) von Mises stress normalized by shear modulus G. (e) Details of (d) in the first 200 s.

It should be noted that, however, experimentally measured $U^{OCP}(x^{Li})$ curves for Li/Si are associated with significant hysteresis (Chevrier and Dahn, 2010) which makes accurate estimate of the quasi-equilibrium value of dU^{OCP}/dx^{Li} difficult. Using the experimental OCP data of Chandrasekaran et al. (2010) and Eq. (59), we estimate that $1 \le \Phi \le 40$ for $2.2 < C^{Li}/C^{Si} < 4.4$ (the composition range studied in this paper). Therefore, the scenario in Figs. 4 and 5(c) reflects the outcome for an unrealistically high value of Φ for Li/Si; instead, the diffusive migration of silicon always leads to stress relaxation in Li/Si and causes Si to migrate along the direction of σ_m gradient [Fig. 3(a)].

4.2. Effect of D^{Si}/D^{Li} and Φ on stress relaxation

Fig. 6 shows how the diffusivity ratio D^{Si}/D^{Li} affects the evolution of the stresses and silicon concentration when the thermodynamic factor is kept at $\Phi=10$. The NW configuration is the same as that in Figs. 3 and 4, with a diameter of 250 nm when fully discharged. The charging rate is 1C under galvanostatic conditions. The normalized silicon concentration C^{Si}/C_0^{Si}, normalized hydrostatic stress σ_m/K and normalized von Mises stress σ_{mises}/G are plotted against time at the NW surface and center (denoted as s and c, respectively). For all D^{Si}/D^{Li} ratios from 0.005 to 0.05, the migration of Si is from the surface to the center, as a result of the dominant effect of $\mathbf{J}^{Si,mech}$ [Fig. 6(a), Eqs. (39)–(41)].

At the very low diffusivity ratio of $D^{Si}/D^{Li}=10^{-8}$, the migration of silicon is essentially negligible. Under this condition, σ_m/K and σ_{mises}/G only change slightly after the initial stress buildup. The analytical solution for $D^{Si}=0$ during the so-called long-term response period after the initial transient buildup is (Gao and Zhou, 2011)

$$\left.\begin{aligned}
\sigma_z &= -\frac{1}{3}\frac{1}{J^{SF}}\frac{\Omega^{Li(SF)}}{\Omega^{Si(SF)}}\frac{E}{1-\nu}\cdot\Delta\xi,\\
\sigma_\theta &= \frac{1}{3}\frac{1}{J^{SF}}\frac{\Omega^{Li(SF)}}{\Omega^{Si(SF)}}\frac{E}{1-\nu}\left(-\Delta\xi+\frac{1}{\tilde r^2}\int_0^{\tilde r}\tilde r\,\Delta\xi\,d\tilde r\right) \quad \text{and}\\
\sigma_r &= -\frac{1}{3}\frac{1}{J^{SF}}\frac{\Omega^{Li(SF)}}{\Omega^{Si(SF)}}\frac{E}{1-\nu}\frac{1}{\tilde r^2}\int_0^{\tilde r}\tilde r\,\Delta\xi\,d\tilde r,
\end{aligned}\right\} \tag{60}$$

where $\Delta\xi(r,t)\equiv\xi-\overline{\xi}$ can be regarded as the composition inhomogeneity, $\xi\equiv C^{Li}/C_0^{Si}$, $\overline{\xi}(t)=4.4(t/T_0)$ is a measure for the average composition over the NW radius and $\tilde r\equiv r/\{[J^{SF}(C_0^{Si},C^{Li})]^{1/3}\rho_0\}$ is the nondimensionalized radius. Obviously, the long-term stresses for $D^{Si}=0$ depend on two factors. The first factor is NW size. As J^{SF} increases due to Li insertion, the stresses may decrease even when $\Delta\xi$ does not change. The second factor is the effective Li diffusivity D_{eff}^{Li}, which depends on the elastic modulus [Eq. (58)]. As Li concentration increases, the Li/Si alloy softens, leading to lower D_{eff}^{Li} and causing the composition inhomogeneity $\Delta\xi$ to change accordingly.

Using the numerical solution for $D^{Si}/D^{Li}=10^{-8}$ or the analytical solution for $D^{Si}=0$ as the reference, we can quantify the effects of Si migration on stress relaxation. The normalized stress invariants σ_m/K and σ_{mises}/G (note that K and G are concentration-dependent and, therefore, decrease with time) first increase during the ramp up of the C^{Li} profile and then decrease as the effect of Si diffusion kicks in. The stresses at the center follow similar trends as the stresses near the surface but lag behind the stresses at the surface because the gradient of the hydrostatic stress $|\partial\sigma_m/\partial X|$ [hence $|\mathbf{J}^{Si,mech}|$ according to Eq. (41)] is higher near the surface than at the center. Note that for $D^{Si}\approx 0$, long-term σ_m/K and σ_{mises}/G change only slightly after $t=12$ s. In contract, the stresses decrease significantly more rapidly at the higher values of D^{Si}. Specifically, for $D^{Si}/D^{Li}=0.02$, the values of σ_m/K and σ_{mises}/G at the surface at $t=1200$ s are both $\sim$20% lower than the corresponding values for $D^{Si}\approx 0$, as well as their corresponding peak values at $t\approx 12$ s. The reductions clearly show that modest mobility of the host atoms (low D^{Si} value of 2×10^{-14} cm^2 s^{-1} or $D^{Si}/D^{Li}=0.02$) can cause stress reductions on the order of $\sim$20% relative to the case without Si mobility. It should be noted that the stress levels here are significantly lower than the yield stress of Li/Si of 1.0–1.75 GPa (Sethuraman et al., 2010). The stress relaxation due to host migration is separate from and in addition to the effects of stress-enhanced diffusion of Li (Gao and Zhou, 2011) and plasticity (Zhao et al., 2011a). Obviously, it can play an important role at high Li concentration levels even when stresses are below the yield threshold of the material.

It is important to note that, for all the D^{Si}/D^{Li} values analyzed, $C^{Si}_{surface}/C^{Si}_0$ at the surface converges to the same steady-state surface value of $\sim$0.996 and C^{Si}_{center}/C^{Si}_0 at the center converges to the same steady-state value of $\sim$1.004. The relaxation (or characteristic) time τ^{Si} for silicon redistribution can be estimated using the time for $(C^{Si}_{center}-\overline{C}^{Si})/C^{Si}_0$ to reach half of its steady-state value, here $\overline{C}^{Si}=C^{Si}_0$ is the average silicon concentration in the NW. According to Fig. 6(a), $\tau^{Si}\approx 210$ s for $D^{Si}=2\times 10^{-14}$ cm^2 s^{-1} ($D^{Si}/D^{Li}=0.02$). The convergences of $C^{Si}_{surface}/C^{Si}_0$ and C^{Si}_{center}/C^{Si}_0 are not by chance. They indicate that Si migration always tends to lead to a steady state which is the same regardless of the value of D^{Si}, as long as $D^{Si}>0$. This steady state is reflected not only in C^{Si}/C^{Si}_0, but also in the stresses. Specifically, σ_m/K converges to the same level of $\sigma_m^{t\gg\tau^{Si}}/K$ at the center and the same level of $-\sigma_m^{t\gg\tau^{Si}}/K$ at the surface [Fig. 6(b)] at $t\gg\tau^{Si}$(e.g., $t/\tau^{Si}>3$). Fig. 6 shows that $\sigma_m^{t\gg\tau^{Si}}/K=0.00054$ for $\Phi=10$. A similar convergence of σ_{mises}/G at long times is seen in Fig. 6(d). It is important to note that the steady-state values of $C^{Si}_{t\gg\tau^{Si}}/C^{Si}_0$ for the surface and the center do evolve slightly as t further increases. This modulation of the steady-state values of $C^{Si}_{t\gg\tau^{Si}}/C^{Si}_0$ at the surface and the center is because of the softening of the elastic modulus as x^{Li} increases, which lowers the mechanical driving force for silicon migration [Eq. (41)]. As seen in Fig. 6(b) and (d), the normalized stresses σ_m/K and σ_{mises}/G decrease accordingly after the transient development of the C^{Si} profile. Parametric study shows that the characteristic time τ^{Si} for achieving the steady state $C^{Si}_{t\gg\tau^{Si}}/C^{Si}_0$ distribution decreases as D^{Si}/D^{Li} increases. This is understandable because $\tau^{Si}\propto 1/D^{Si}$. It should be noted that, however, τ^{Si} cannot be simply estimated as $\rho^2/\lambda_1^2D^{Si}$ using the tracer diffusivity D^{Si}, because such an estimation does not reflect the fact that Si diffusion is affected by the migration of Li through the stress driving forces and the Li–Si chemical interactions. Indeed, $\rho^2/\lambda_1^2D^{Si}\sim 2\times 10^3$ s for $D^{Si}=2\times 10^{-14}$ cm^2 s^{-1} if the diffusion of Si occurs independently by itself without the presence of Li and without SED. Rather, it is the effective diffusivity D^{Si}_{eff} of Si, that determines τ^{Si}. Although a closed-form solution for D^{Si}_{eff} may not be easily obtained [in contrast, D^{Li}_{eff} which is analytically quantified in Eq. (58)], the numerical results here indicate that $D^{Si}_{eff}\gg D^{Si}$ due to the strong coupling between stress and interdiffusion, at least for the case of $\Phi=10$.

Fig. 7 illustrates the effect of Φ at a constant diffusivity ratio of $D^{Si}/D^{Li}=0.02$. Again, the NW radius is 250 nm at the fully discharged state and the charging rate is 1C. The most important observation is that the direction of Si migration changes as Φ changes. Specifically, Si migrates from the surface to the center for $5<\Phi<40$ and from the center to the surface for $\Phi=90$ [see Fig. 7(a)]. The reversal occurs at a critical value Φ_{cr}, when $\mathbf{J}^{Si,mech}$ and $\mathbf{J}^{Si,chem}$ happen to cancel each other out. It should be noted that $|\mathbf{J}^{Si,mech}|$ depends on the magnitude of the elastic modulus, which decreases as lithium concentration increases. Therefore, the critical value Φ_{cr} is not a constant. A typical value is found to be approximately $\Phi_{cr}=50$. When Φ is close to $\Phi_{cr}=50$, silicon migration is insignificant since $\mathbf{J}^{Si,mech}+\mathbf{J}^{Si,chem}$ is very small, although it may not be exactly zero.

When $\Phi<\Phi_{cr}$, stresses first increase and then decrease gradually after reaching respective peaks [Fig. 7(b–e)]. When $\Phi>\Phi_{cr}$, on the other hand, Si migrates in the opposite direction and stresses increase monotonically after the initial fast buildup. For $5<\Phi<40$, C^{Si}/C^{Si}_0 evolves towards a Φ-dependent value of $C^{Si}_{t\gg\tau^{Si}}/C^{Si}_0$. The difference between the center and surface values of $C^{Si}_{t\gg\tau^{Si}}/C^{Si}_0$ is larger when Φ is smaller. The peak values of stresses are higher at lower Φ, i.e., the stress relaxation due to Si migration is more significant when the thermodynamic factor is lower (or the host and guest are less likely to chemically mix).

Interestingly, although stresses evolve significantly differently for $\Phi>\Phi_{cr}$ and $\Phi<\Phi_{cr}$, they all converge to the same values [Fig. 7(b) and (d)] at sufficiently long times. The similar convergence behavior has also been seen in Fig. 6(b) and (d). A comparison between Fig. 7(b) and (d) with Fig. 6(b) and (d) reveals that the long-term stress limits are quite universal, regardless of the values of Φ and D^{Si}/D^{Li}.

An analysis provides useful insight. As the distribution of C^{Si} approaches the steady-state, the silicon flux vanishes, i.e.,

$$\mathbf{J}^{Si}\approx 0 \quad \text{at} \quad t\gg\tau^{Si} \tag{61}$$

Eqs. (39) and (61) lead to

$$\Phi\nabla_{\mathbf{X}}x^{Si}_{t\gg\tau^{Si}}-\frac{x^{Si}_{t\gg\tau^{Si}}\Omega^{Si(SF)}}{k_B\theta}\nabla_{\mathbf{X}}\sigma_m^{t\gg\tau^{Si}}\approx 0 \quad \text{at} \quad t\gg\tau^{Si}. \tag{62}$$

This equation is independent of D^{Si} as it concerns the steady-state solution of x^{Si} for $t\gg\tau^{Si}$. Eq. (62) shows that x^{Si}, hence C^{Si}, for $t\gg\tau^{Si}$ does depend on the value of Φ, providing a direct proof for what is seen in Fig. 7(a). On the other hand, since the spatial gradient $\nabla C^{Li}(r,t)$ remains approximately a constant (the C^{Li} profile "shifts" upward without changing its shape)

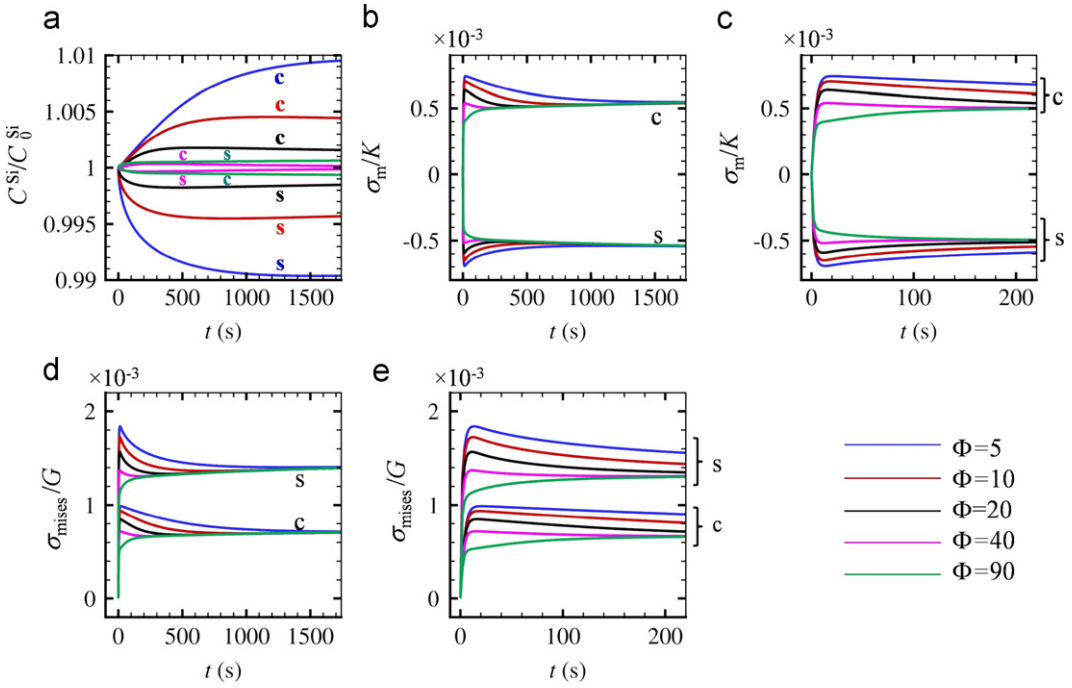

Fig. 7. Evolution of silicon concentration and stress invariants at the NW center (denoted as c) and surface (denoted as s) at different values of Φ between 5 and 90. The diffusivity ratio is kept at $D^{Si}/D^{Li}=0.02$. All other parameters are the same as those in Fig. 3. (a) Lagrangian silicon concentration C^{Si} normalized by C_0^{Si}. (b) Hydrostatic stress σ_m normalized by bulk modulus K; (c) details of (b) in the first 200 s. (d) von Mises stress σ_{mises} normalized by shear modulus G. (e) Details of (d) in the first 200 s.

at $t \gg \tau^{Li}$ (Gao and Zhou, 2011)

$$\nabla_{\mathbf{X}}\mathbf{J}^{Li} = -\frac{\partial C^{Li}}{\partial t} = -\frac{4.4C_0^{Si}}{T_0} = constant, \quad \text{at } t \gg \tau^{Li}, \tag{63}$$

where $4.4C_0^{Si}$ is the Li concentration at the fully charged state and T_0 is the total galvanostatic charging time to attain full charge. If high-order terms are neglected, Eqs. (63) and (39) lead to

$$D^{Li}\nabla_{\mathbf{X}}\cdot\left[-\Phi\nabla_{\mathbf{X}}x^{Li} + \frac{\Omega^{Li(SF)}}{k_B\theta}x^{Li}\nabla_{\mathbf{X}}\sigma_m\right] = constant \quad \text{at } t \gg \tau^{Li} \tag{64}$$

Eqs. (62) and (64) and the fact that $\tau^{Si} > \tau^{Li}$ combine to give

$$D^{Li}\nabla_{\mathbf{X}}\cdot\left[-\Phi\nabla_{\mathbf{X}}(x^{Li}+x^{Si}) + \left(\frac{\Omega^{Li(SF)}x^{Li}}{k_B\theta} + \frac{\Omega^{Si(SF)}x^{Si}}{k_B\theta}\right)\nabla_{\mathbf{X}}\sigma_m\right] = constant \quad \text{at } t \gg \tau^{Si}. \tag{65}$$

Since $\nabla_X(x^{Li}+x^{Si})=0$, the above leads to a Φ-independent equation for σ_m in the form of

$$D^{Li}\nabla_{\mathbf{X}}\cdot\left[\left(\frac{\Omega^{Li(SF)}x^{Li}}{k_B\theta} + \frac{\Omega^{Si(SF)}x^{Si}}{k_B\theta}\right)\nabla_{\mathbf{X}}\sigma_m\right] = constant \quad \text{at } t \gg \tau^{Si}. \tag{66}$$

Eqs. (62) and (66) indicate that the steady-state hydrostatic stress depends on neither D^{Si}/D^{Li} nor Φ. By extension via Eqs. (31), (34) and (36), all stress components at the steady-state are independent of D^{Si}/D^{Li} and Φ, as long as stressing is entirely due to concentration inhomogeneity and no external mechanical load is applied, as is the case of the free-standing NW analyzed here. It is important to note that the peak values of the stresses do depend on Φ, as Fig. 7 shows. Also, the relaxation time needed for the solutions to converge to the steady-state depends on D^{Si}/D^{Li}. Again, for $\Phi=10$ and $D^{Si}/D^{Li}=0.02$ the stress reduction from the level without Si migration can amount to 20%. Even for the small diffusivity ratio of $D^{Si}/D^{Li}=0.005$, the host-diffusion-induced stress relaxation is non-negligible [Fig. 6(b) and (d)]. Therefore, account should be taken for host migration in the analyses of Li/Si electrodes.

5. Concluding remarks

A finite deformation framework is developed and used to model the coupled mechanical–diffusional response of Li alloy-based electrodes under conditions of electrical equilibrium. The framework accounts for elastic material response

and the diffusion of both guest and host species. A novel numerical framework with mixed finite elements is developed to solve the underlying equations, allowing the coupled mechanical and diffusional processes to be analyzed. To evaluate the gradient of pressure required in the calculation of the diffusion fluxes, the method takes displacement, host/guest concentrations and hydrostatic stress as independent nodal variables and uses a Lagrangian multiplier to ensure that the hydrostatic stress field satisfies the constitutive equations.

Calculations carried out focus on the effects of host migration on the relaxation of stress and changes in the concentrations of both the host and guest species. It is found that diffusion of the host atoms can have a significant impact on stress, primarily because of the chemical interactions between the species and the effect of stress gradient on interdiffusion. In particular, under conditions of pure elastic deformation the diffusion of Si atoms can cause stress reductions up to 20% with the modest diffusivity ratio of $D^{Si}/D^{Li}=1/50$ ($D^{Li}=100$ nm^2/s and $D^{Si}=2$ nm^2/s). For amorphous Li/Si alloys, the mechanical driving force dominates the chemical driving force, resulting in the migration of Si in the direction of the gradient of the hydrostatic stress $\nabla\sigma_m$ or from the surface to the center of cylindrical electrodes. The analysis has also shown what the behavior would be for alloys with (perhaps unrealistically) high thermodynamic factors. The results indicate that the effect of interdiffusion on stress relaxation can be important even when the stress levels are below the yield threshold of the material.

The migrations of the host and guest introduce two time scales. The time scale for host migration is much longer than the time scale for guest migration, allowing the distribution of guest concentration to reach its own steady state which is slowly modulated by other factors, especially the migration of the host. The time scale for host migration determines the rate at which the ultimate steady state of host concentration and all other field quantities are attained. The distribution of Si concentration is determined by the thermodynamic factor which measures the tendency for the host and guest to chemically mix, but the steady-state stress distribution depends on neither D^{Si}/D^{Li} nor the thermodynamic factor.

Finite diffusivity values of host atoms may have further implications besides the relaxation of stresses. For example, in Li/Si and Li/Ge nano-electrodes, cycling-induced formation of nano-pores indicates that the host material has been irreversibly moved away from the voided regions (Hu et al., 2011; Liu et al., 2011a). If reversible expansion and elastic deformation were the only mechanisms for material deformation, the nano-pores would not form because the host network must revert back to its original configuration upon unloading. Two mechanisms have been proposed to account for the irreversible migration of host atoms. The first is inelastic flow (a form of continuous convection) driven by deviatoric stresses during which material flows in the normal direction of the nucleated pore, leading to void enlargement (Hu et al., 2011). The second mechanism is vacancy aggregation during selective dealloying, which involves diffusive migration of host atoms and allows nucleated voids to coalesce and grow (Liu et al., 2011a). Either or both mechanisms might be relevant, their relative significance depends on the specific material system. With minor adaptation, the continuum framework developed here can be used to delineate the influences of these mechanisms on void development under various conditions.

Acknowledgment

Support from the National Research Foundation of Korea through WCU Grant no. R31-2009-000-10083-0 is acknowledged. M.Z. would like to thank Dr. Yue Qi for enlightening discussions and for providing the data on Si and Li diffusivities. Y.F.G. would like to thank Dr. Ting Zhu for helpful discussions.

References

Abu Al-Rub, R.K., Voyiadjis, G.Z., 2005. A direct finite element implementation of the gradient-dependent theory. Int. J. Numer. Methods Eng. 63, 603–629.
Argon, A.S., Demkowicz, M.J., 2008. What can plasticity of amorphous silicon tell us about plasticity of metallic glasses? Metall. Mater. Trans. A 39A, 1762–1778.
Aziz, M.J., Sabin, P.C., Lu, G.Q., 1991. The activation strain tensor—nonhydrostatic stress effects on crystal-growth kinetics. Phys. Rev. B. 44, 9812–9816.
Beaulieu, L.Y., Eberman, K.W., Turner, R.L., Krause, L.J., Dahn, J.R., 2001. Colossal reversible volume changes in lithium alloys. Electrochem. Solid State Lett. 4, A137–A140.
Beaulieu, L.Y., Hatchard, T.D., Bonakdarpour, A., Fleischauer, M.D., Dahn, J.R., 2003. Reaction of Li with alloy thin films studied by in situ AFM. J. Electrochem. Soc. 150, A1457–A1464.
Borja, R.I., Tamagnini, C., Alarcon, E., 1998. Elastoplastic consolidation at finite strain. Part 2: finite element implementation and numerical examples. Comput. Method Appl. Mech. Eng. 159, 103–122.
Bower, A.F., Guduru, P.R., Sethuraman, V.A., 2011. A finite strain model of stress, diffusion, plastic flow, and electrochemical reactions in a lithium-ion half-cell. J. Mech. Phys. Solids 59, 804–828.
Chan, C.K., Peng, H.L., Liu, G., McIlwrath, K., Zhang, X.F., Huggins, R.A., Cui, Y., 2008. High-performance lithium battery anodes using silicon nanowires. Nat. Nanotechnol. 3, 31–35.
Chandrasekaran, R., Magasinski, A., Yushin, G., Fuller, T.F., 2010. Analysis of lithium insertion/deinsertion in a silicon electrode particle at room temperature. J. Electrochem. Soc. 157, A1139–A1151.
Cheng, Y.T., Verbrugge, M.W., 2008. The influence of surface mechanics on diffusion induced stresses within spherical nanoparticles. J. Appl. Phys. 104, 083521.
Chevrier, V.L., Dahn, J.R., 2010. First principles studies of disordered lithiated silicon. J. Electrochem. Soc. 157, A392–A398.
Choi, J.W., McDonough, J., Jeong, S., Yoo, J.S., Chan, C.K., Cui, Y., 2010. Stepwise nanopore evolution in one-dimensional nanostructures. Nano Lett. 10, 1409–1413.
Chon, M.J., Sethuraman, V.A., McCormick, A., Srinivasan, V., Guduru, P.R., 2011. Real-time measurement of stress and damage evolution during initial lithiation of crystalline silicon. Phys. Rev. Lett. 107.
Christensen, J., Newman, J., 2006. Stress generation and fracture in lithium insertion materials. J. Solid State Electr. 10, 293–319.
Cogswell, D.A., Bazant, M.Z., 2012. Coherency strain and the kinetics of phase separation in $LiFePO_4$ nanoparticles. ACS Nano 6, 2215–2225.

Cui, L.F., Ruffo, R., Chan, C.K., Peng, H.L., Cui, Y., 2009. Crystalline-amorphous core-shell silicon nanowires for high capacity and high current battery electrodes. Nano Lett. 9, 491–495.
Deshpande, R., Cheng, Y.T., Verbrugge, M.W., 2010. Modeling diffusion-induced stress in nanowire electrode structures. J. Power Sources 195, 5081–5088.
Ding, N., Xu, J., Yao, Y.X., Wegner, G., Fang, X., Chen, C.H., Lieberwirth, I., 2009. Determination of the diffusion coefficient of lithium ions in nano-Si. Solid State Ionics 180, 222–225.
Gao, Y.F., Zhou, M., 2011. Strong stress-enhanced diffusion in amorphous lithium alloy nanowire electrodes. J. Appl. Phys. 109, 014310.
Garcia, R.E., Chiang, Y.M., Carter, W.C., Limthongkul, P., Bishop, C.M., 2005. Microstructural modeling and design of rechargeable lithium-ion batteries. J. Electrochem. Soc. 152, A255–A263.
Haftbaradaran, H., Gao, H.J., Curtin, W.A., 2010. A surface locking instability for atomic intercalation into a solid electrode. Appl. Phys. Lett. 96, 091909.
Hertzberg, B., Benson, J., Yushin, G., 2011. Ex-situ depth-sensing indentation measurements of electrochemically produced Si–Li alloy films. Electrochem. Commun. 13, 818–821.
Hu, L., Wu, H., Gao, Y., Cao, A., Cui, L., McDough, J., Xie, X., Zhou, M., Cui, Y., 2011. Silicon–carbon nanotube coaxial sponge as Li-ion anodes with high areal capacity. Adv. Energy Mater., 523–527.
Huang, S., Zhu, T., 2011. Atomistic mechanisms of lithium insertion in amorphous silicon. J. Power Sources 196, 3664–3668.
Johari, P., Qi, Y., Shenoy, V.B., 2011. The mixing mechanism during lithiation of Si negative electrode in Li-ion batteries: an ab lnitio molecular dynamics study. Nano Lett. 11, 5494–5500.
Kao, Y., Tang, M., Meethong, N., Bai, J., Carter, W., Chiang, Y., 2010. Overpotential-dependent phase transformation pathways in lithium iron phosphate battery electrodes. Chem. Mater. 22, 5845–5855.
Kim, H., Chou, C.Y., Ekerdt, J.G., Hwang, G.S., 2011. Structure and properties of Li–Si alloys: a first-principles study. J. Phys. Chem. C 115, 2514–2521.
Kim, H., Kweon, K.E., Chou, C.Y., Ekerdt, J.G., Hwang, G.S., 2010. On the nature and behavior of Li atoms in Si: a first principles study. J. Phys. Chem. C 114, 17942–17946.
Larcher, D., Beattie, S., Morcrette, M., Edstroem, K., Jumas, J.C., Tarascon, J.M., 2007. Recent findings and prospects in the field of pure metals as negative electrodes for Li-ion batteries. J. Mater. Chem. 17, 3759–3772.
Lee, E.H., 1981. Some comments on elastic–plastic analysis. Int. J. Solids Struct. 17, 859–872.
Li, J.C., Dozier, A.K., Li, Y.C., Yang, F.Q., Cheng, Y.T., 2011. Crack pattern formation in thin film lithium–ion battery electrodes. J. Electrochem. Soc. 158, A689–A694.
Limthongkul, P., Jang, Y.I., Dudney, N.J., Chiang, Y.M., 2003. Electrochemically-driven solid-state amorphization in lithium-silicon alloys and implications for lithium storage. Acta Mater. 51, 1103–1113.
Liu, X.H., Huang, S., Picraux, S.T., Li, J., Zhu, T., Huang, J.Y., 2011a. Reversible nanopore formation in Ge nanowires during lithiation-delithiation cycling: an in situ transmission electron microscopy study. Nano Lett. 11, 3991–3997.
Liu, X.H., Zheng, H., Zhong, L., Huan, S., Karki, K., Zhang, L.Q., Liu, Y., Kushima, A., Liang, W.T., Wang, J.W., Cho, J.H., Epstein, E., Dayeh, S.A., Picraux, S.T., Zhu, T., Li, J., Sullivan, J.P., Cumings, J., Wang, C.S., Mao, S.X., Ye, Z.Z., Zhang, S.L., Huang, J.Y., 2011b. anisotropic swelling and fracture of silicon nanowires during lithiation. Nano Lett. 11, 3312–3318.
Luscher, D.J., McDowell, D.L., Bronkhorst, C.A., 2010. A second gradient theoretical framework for hierarchical multiscale modeling of materials. Int. J. Plasticity 26, 1248–1275.
Magasinski, A., Dixon, P., Hertzberg, B., Kvit, A., Ayala, J., Yushin, G., 2010. High-performance lithium–ion anodes using a hierarchical bottom-up approach. Nat. Mater. 9, 353–358.
Pell, E.M., 1960. Diffusion of Li in Si at high-T and the isotope effect. Phys. Rev. 119, 1014–1021.
Purkayastha, R., McMeeking, R.M., 2012. A linearized model for lithium ion batteries and maps for their performance and failure. J. Appl. Mech. T. ASME 79.
Ruffo, R., Hong, S.S., Chan, C.K., Huggins, R.A., Cui, Y., 2009. Impedance analysis of silicon nanowire lithium ion battery anodes. J. Phys. Chem. C 113, 11390–11398.
Ryu, I., Choi, J.W., Cui, Y., Nix, W.D., 2011. Size-dependent fracture of Si nanowire battery anodes. J. Mech. Phys. Solids 59, 1717–1730.
Sethuraman, V.A., Chon, M.J., Shimshak, M., Srinivasan, V., Guduru, P.R., 2010. In situ measurements of stress evolution in silicon thin films during electrochemical lithiation and delithiation. J. Power Sources 195, 5062–5066.
Shenoy, V.B., Johari, P., Qi, Y., 2010. Elastic softening of amorphous and crystalline Li–Si Phases with increasing Li concentration: a first-principles study. J. Power Sources 195, 6825–6830.
Shu, J.Y., King, W.E., Fleck, N.A., 1999. Finite elements for materials with strain gradient effects. Int. J. Numer. Methods Eng. 44, 373–391.
Song, T., Xia, J.L., Lee, J.H., Lee, D.H., Kwon, M.S., Choi, J.M., Wu, J., Doo, S.K., Chang, H., Il Park, W., Zang, D.S., Kim, H., Huang, Y.G., Hwang, K.C., Rogers, J.A., Paik, U., 2010. Arrays of sealed silicon nanotubes as anodes for lithium ion batteries. Nano Lett. 10, 1710–1716.
Stephenson, G.B., 1988. Deformation during interdiffusion. Acta Metall. 36, 2663–2683.
Swaminathan, N., Qu, J., Sun, Y., 2007. An electrochemomechanical theory of defects in ionic solids. I. Theory. Philos. Mag. 87, 1705–1721.
Szabadi, M., Hess, P., Kellock, A.J., Coufal, H., Baglin, J.E.E., 1998. Elastic and mechanical properties of ion-implanted silicon determined by surface-acoustic-wave spectrometry. Phys. Rev. B 58, 8941–8948.
Tang, M., Carter, W., Belak, J., Chiang, Y., 2010a. Modeling the competing phase transition pathways in nanoscale olivine electrodes. Electrochim. Acta 56, 969–976.
Tang, M., Carter, W., Chiang, Y., Clarke, D., Ruhle, M., Zok, F., 2010b. Electrochemically driven phase transitions in insertion electrodes or lithium–ion batteries: examples in lithium metal phosphate olivines. Ann. Rev. Mater. Res. 40 (40), 501–529.
Van der Ven, A., Garikipati, K., Kim, S., Wagemaker, M., 2009. The role of coherency strains on phase stability in Li(x)FePO(4): needle crystallites minimize coherency strain and overpotential. J. Electrochem. Soc. 156, A949–A957.
Van der Ven, A., Yu, H.C., Ceder, G., Thornton, K., 2010. Vacancy mediated substitutional diffusion in binary crystalline solids. Prog. Mater. Sci. 55, 61–105.
Wu, C.H., 2001. The role of Eshelby stress in composition-generated and stress-assisted diffusion. J. Mech. Phys. Solids 49, 1771–1794.
Xiao, X., Liu, P., Verbrugge, M.W., Haftbaradaran, H., Gao, H., 2011. Improved cycling stability of silicon thin film electrodes through patterning for high energy density lithium batteries. J. Power Sources 196, 1409–1416.
Xie, J., Imanishi, N., Zhang, T., Hirano, A., Takeda, Y., Yamamoto, O., 2010. Li-ion diffusion in amorphous Si films prepared by RF magnetron sputtering: a comparison of using liquid and polymer electrolytes. Mater. Chem. Phys. 120, 421–425.
Yu, H.H., Suo, Z., 2000. Stress-dependent surface reactions and implications for a stress measurement technique. J. Appl. Phys. 87, 1211–1218.
Zhang, X.C., Shyy, W., Sastry, A.M., 2007. Numerical simulation of intercalation-induced stress in Li-ion battery electrode particles. J. Electrochem. Soc. 154, A910–A916.
Zhao, K.J., Pharr, M., Vlassak, J.J., Suo, Z., 2011a. Large plastic deformation in high-capacity lithium–ion batteries caused by charge and discharge. J. Am. Ceram. Soc. 94, s226–s235.
Zhao, K.J., Pharr, M., Vlassak, J.J., Suo, Z.G., 2011b. Inelastic hosts as electrodes for high-capacity lithium–ion batteries. J. Appl. Phys. 109, 016110.
Zhou, H.G., Qu, J.M., Cherkaoui, M., 2010. Stress-oxidation interaction in selective oxidation of Cr–Fe alloys. Mech. Mater. 42, 63–71.
Zienkiewicz, O.C., Taylor, R.L., 2000. The Finite Element Method, fifth ed. Butterworth-Heinemann, Oxford, Boston.